EVAPORATIVE COOLING EFFECTS IN PRECISION MACHINE TOOLS

by

Carsie Alvin Hall, III

Bachelor of Science in Mechanical Engineering
Howard University (1990)

Master of Engineering
Howard University (1992)

Submitted to the Department of Mechanical Engineering
in Partial Fulfillment of the Requirements for the Degree of

Master of Science in Mechanical Engineering

at the

MASSACHUSETTS INSTITUTE OF TECHNOLOGY

February 1995

Author.....................
Department of Mechanical Engineering
January 12, 1995

Certified by.....................
John H. Lienhard V, Associate Professor
Thesis Supervisor

Accepted by.....................
Ain A. Sonin, Chairman
Departmental Committee on Graduate Studies

Evaporative Cooling Effects in Precision Machine Tools

by

Carsie Alvin Hall, III

Submitted to the Department of Mechanical Engineering on January 12, 1995,
in Partial Fulfillment of the Requirements for the Degree of
Master of Science in Mechanical Engineering

Abstract

Thermal deflections or thermal bending errors in precision machine tools subject to evaporative cooling have been predicted analytically and numerically. Evaporative cooling is provided using water. Solutions are provided for two cases: 1) no water flow (static) across the machine tool surface and 2) water flow at a constant mass flow rate across the tool surface. The effects of relative humidity (in the range: 0-100 %) and ambient temperature (in the range: 15-35 °C) are examined in detail. In addition, the effect of the average convective heat transfer coefficient of air (in the range: 5-25 W/m²°C) across the water surface is examined. The water level on the tool surface is maintained steady at values typically on the order of 1 mm.

It was determined that maximum thermal deflections occur in the no flow case, with deflections on the order of tens to hundreds of microns. Maximum deflections also occur at lower ambient temperatures (relative to the temperature of the hot-side machine tool surface) and high values of the average convective heat transfer coefficient. Therefore, in the no flow case, it is desirable to avoid dry air conditions, and the average convective heat transfer coefficient of air should be kept low. This means suppressing the effects of free convection in the room housing the machine tool. In the flow case, minimum deflections occur at high flow rates, as the machine tool is driven to an isothermal state.

Thesis Supervisor: John H. Lienhard V
Title: Associate Professor
                       Department of Mechanical Engineering
                       Warren M. Rohsenow Heat and Mass Transfer Laboratory

Acknowledgments

Dedication

To my family, living and deceased

Table of Contents

Chapter 1

Chapter 2:   Mathematical Modeling

Chapter 3:   Hydrostatic Model

Chapter 4:   Hydrodynamic Model

Chapter 5

List of Figures

Chapter 1

1.1 Introduction

Thermal errors are a major source of the total system error budget in precision machine tools. Thermal gradients in the system are the cause of thermal bending errors in machine tool members. In an ideal system, the machine will warm up to a uniform temperature during steady-state operation. However, due to the continuous operation of motors, high-speed spindles, and other devices with moving parts (frictional heating), a non-uniform temperature distribution results. Other sources that contribute to thermal gradients in the system include friction in the material cutting process and the external environment through incandescent lighting, radiation heating via a window, heating or cooling ducts, the floor, and the operator's own body heat. The various heat transfer mechanisms that allow for thermal gradients are conduction, convection, radiation, and evaporation (Slocum, 1992).

In general, there are three common types of errors: 1) random, 2)systematic, and 3) hysteresis. Slocum (1992) categorizes thermal errors as a kind of quasi-static mechanical error. Other error types include geometric, kinematic, external load-induced (caused by gravity loads, accelerating axes, and cutting forces), machine assembly load-induced, material instability, and instrumentation errors. These errors are considered to occur relatively slowly, at a frequency much lower than the bandwidth of axes on the machine that could be used to correct the errors.

Precision machine tools employing water hydrostatic bearings are often subject to evaporative cooling as a result of leakage flow from the bearings. The Hydroguide™, a hydrostatic, self-compensating water bearing is one such example. Evaporative cooling serves to lower the temperature of the surface on which the water is in contact, resulting in thermal deformation of the machine tool member. Water is preferred to oil due to its relatively lower viscosity (resulting in lower viscous heat dissipation and temperature rise at higher speeds) and its environmental acceptance (i.e. it is not a fire hazard). It also has a higher heat capacity, which results in a lower temperature rise.

1.2 Scope of Work

This thesis work concerns the analytic and numerical prediction of thermal deflection of machine tool members subject to evaporative cooling. The machine tool member, throughout this work, is modeled as a homogenous, isotropic, linearly elastic beam. The relative effects of water mass flow rate (varied between 0 and 80 g/s) across the beam surface, average convective heat transfer coefficient (5 and 25 W/m^2°C) of air across the water layer, relative humidity (varied between 0 and 100%), ambient air temperature (15, 25, and 35 °C), and uniform hot-side surface temperature (25 and 35 °C) are investigated. It is assumed that the machine tool designer has control of these parameters. Three models are presented: 1) a hydrostatic model, 2) a 1-D hydrodynamic model, and 3) a 2-D hydrodynamic model. Fig. 1.1 depicts the physical configuration used throughout this study. This model, for example, simulates the thermal bending errors in machine tool carriages employing linear hydrostatic opposed pad bearings (Slocum, 1992, pg. 552) with continous flow of water from the bearings. This model can also be used to simulate thermal bending errors in shafts supported by linear hydrostatic journal bearings provided the bearing gap is small compared to the shaft radius. For the hydrostatic model (no water flow), a typical design algorithm is presented.

Throughout the hydrodynamic case study, the Hydroguide™ dimensions (L=1.37 m and H=0.0635 m) and thermal properties (α'=6 µm/m°C and k_t=1.6 W/m°C for granite) are used. This fixes the beam aspect ratio at L/H=21.57. Numerical results are presented in the form of various dimensionless plots, temperature contours, and distributions of temperature and thermal deflection along the beam. In addition, some analytic expressions are presented for the hydrostatic case and the 1-D hydrodynamic case. For the 2-D hydrodynamic case, the temperature distribution in the beam is calculated using the standard 2-D equation for steady-state heat conduction in the absence of sinks or souces (Laplace's equation), coupled with the differential equation for the temperature distribution of the air-water interface (Ricatti's equation). This results in a nonlinear boundary condition in the formulation of the 2-D model. The 2-D domain is discretized using finite difference techniques and the resulting equations solved simultaneously.

$$T_{air}$$

water inlet at T_h evaporation rate $\dot{m}''$ T_s water layer   h

MACHINE TOOL MEMBER   H

L T_h
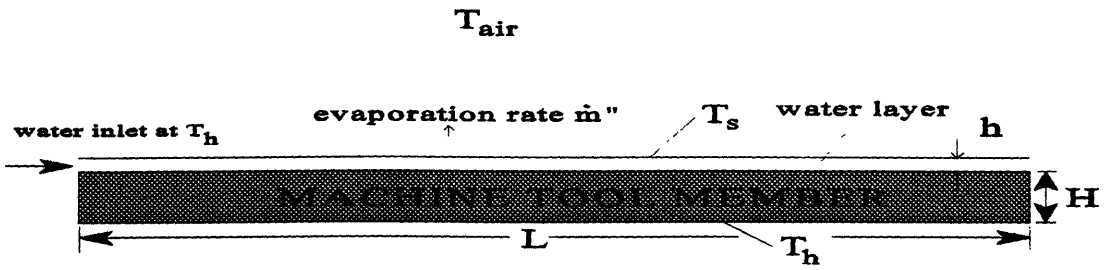
Fig. 1.1 Physical model of machine tool member subject to evaporative cooling.

Chapter 2
Mathematical Modeling

2.1 Fundamentals of Evaporative Cooling

Evaporation is a process by which liquid molecules near a gas-liquid interface experience collisions that increase their energy above that which is necessary to overcome the surface binding energy. The required energy to sustain the evaporation process comes from the internal energy of the liquid, which, as a result, lowers the temperature and produces the cooling effect (Incropera and DeWitt, 1981). The energy associated with this phase change is the latent heat of vaporization of the liquid, which represents the amount of energy required to convert a unit mass of liquid to vapor.

In order to predict the amount of evaporation from a liquid surface, one must understand the underlying physical mechanisms and begin to quantify the parameters relevant to this phenomenon. Mass transfer is analogous to heat transfer in relation to their respective driving forces. In heat transfer, temperature difference is the driving force; in mass transfer, concentration difference is the driving force.

The evaporation rate or the total mass transfer rate to or from the liquid surface is given by (Lienhard, 1987)

$$\dot{m}'' = g_i \, B_i \tag{2.1.1}$$

where

$$B_i = \left(\frac{m_{i,e} - m_{i,s}}{m_{i,s} - 1} \right) \tag{2.1.2}$$

for a single species i transferred. Here, g_i is the mass transfer coefficient, B_i is the mass transfer driving factor, $m_{i,e}$ and $m_{i,s}$ are the mass fractions of vapor far away in the free

12

stream and near the gas-liquid interface, respectively. The expressions for the mass fractions of vapor are

$$m_{i,e} = \frac{X_{h_2o,e} \, M_{h_2o}}{X_{h_2o,e} \, M_{h_2o} + (1 - X_{h_2o,e})M_{air}} \qquad (2.1.3)$$

$$m_{i,s} = \frac{X_{h_2o,s} \, M_{h_2o}}{X_{h_2o,s} \, M_{h_2o} + (1 - X_{h_2o,s})M_{air}} \qquad (2.1.4)$$

for an air-water mixture. $X_{h_2o,e}$ and $X_{h_2o,s}$ are the mole fractions of water vapor far away in the free stream and near the air-water interface, respectively. M_{h_2o} and M_{air} are the molecular weights of water and air, given numerically as 18.02 and 28.97, respectively. In addition, the mole fractions of vapor are expressed as

$$X_{h_2o,e} = \frac{\phi \, P_{sat}(T_{air})}{P_{atm}} \qquad (2.1.5)$$

$$X_{h_2o,s} = \frac{P_{sat}(T_s)}{P_{atm}} \qquad (2.1.6)$$

where ϕ is the relative humidity, $P_{sat}(T_{air})$ is the saturation pressure of water vapor at the atmospheric air temperature, $P_{sat}(T_s)$ is the saturation pressure of water vapor at the air-water interface temperature, and P_{atm} is the local atmospheric pressure.

The mass transfer coefficient g_i is often approximated by a low-rate mass transfer coefficient defined as (Lienhard, 1987)

13

$$g^*_i = \lim_{\dot{m}'' \to 0} g_i \qquad\qquad (2.1.7)$$

Eqn. 2.1.7 is an excellent approximation when mass transfer rates are low (i.e. mass transfer is dominated by the diffusion process). The relationship between g_i and g^*_i is derived as

$$g_i = g^*_i \left[\frac{\ln (1 + B_i)}{B_i} \right] \qquad\qquad (2.1.8)$$

which, in the limit of small values of B_i, reduces to $g_i \cong g^*_i$. As a result, Eqn. 2.1.1 becomes

$$\dot{m}'' \cong g^*_i B_i \qquad\qquad (2.1.9)$$

The low-rate mass transfer coefficient g^*_i is calculated using the heat and mass transfer analogy, given by

$$g^*_i = \frac{h^*}{c_p} Le^{2/3} \qquad\qquad (2.1.10)$$

where h^* is the heat transfer coefficient at zero net mass transfer, c_p is specific heat of the liquid, and Le is the Lewis number ($Le = D_{im}/\alpha$). D_{im} is the binary diffusion coefficient and α is the thermal diffusivity. For air-water systems, $Le \cong 1.18$.

14

2.2 Fundamentals of Linear Elastic Beam Theory

Free beams subject to end bending moments, in the absence of other external loads, undergo deflections according to (Johns, 1965)

$$\frac{d^2v}{dx^2} = c \qquad (2.2.1)$$

where v is the deflection normal to the beam neutral axis, x is the coordinate aligned along the beam neutral axis, and c is the beam curvature. It is required that the net axial force and moment on each cross-section be zero. Fig. 2.1 shows the beam cross-section and the orientation of the coordinate axes.
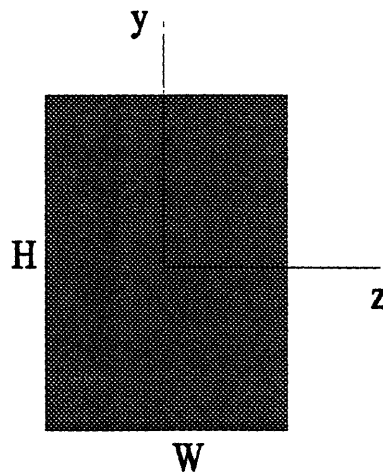
Fig. 2.1 Beam cross-section; x-direction is normal to the page.

In solving problems of this nature, it is assumed that "plane cross-sections remain plane and perpendicular to the beam axis during the given loading and/or heating" and "distortion of the cross-section due to Poisson's ratio effects is negligible." The curvature that corresponds to deflections in the y-direction (Eqn. 2.2.1) is given by

$$c = - \frac{M_{zz}}{\overline{EI_{zz}}}$$

(2.2.2)

$$\overline{EI_{zz}} = \int Ey^2 dA$$

(2.2.3)

where E is the modulus of elasticity, I_{zz} is moment of inertia about the z-axis, dA is the differential cross-sectional area, M_{zz} is the themo-elastic moment about the z-axis, where for an arbitrary temperature distribution T(x,y,z), is expressed as

$$M_{zz} = \int E\alpha' T(y-y^*) dA$$

(2.2.4)

where α' is the thermal expansion coefficient and y* is the y-coordinate of the position of the elastic centroid. With reference to Fig. 2.1, the centroid is located at (y*,z*)=(0,0) since this location corresponds to the origin of the coordinate axes.

Substituting Eqns. 2.2.2-2.2.4 into Eqn. 2.2.1, with the appropriate limits of integration, results in the following:

$$\frac{d^2v}{dx^2} = \frac{- \alpha' \int_{-H/2}^{H/2} T(x,y)y dy}{\int_{-H/2}^{H/2} y^2 dy}$$

(2.2.5)

16

for constant material properties and a 2-D temperature distribution T(x,y). Eqn. 2.2.5 can further be non-dimensionalized using the beam height H as follows:

$$x' = \frac{x}{H} \quad , \; y' = \frac{y}{H} \quad , \; v' = \frac{v}{H}$$

(2.2.6)

Upon introducing these non-dimensional quantities into Eqn. 2.2.5, the dimensionless equation for the distribution of deflection in the y-direction, subject to an arbitrary 2-D temperature distibution T(x',y'), is given as

$$\frac{d^2v'}{dx'^2} = \frac{-\alpha' \int_{-1/2}^{1/2} T(x'\!,y')y'dy'}{\int_{-1/2}^{1/2} y'^2 dy'}$$

(2.2.7)

where upon evaluating the integral in the denominator, Eqn. 2.2.7 reduces to

$$\frac{d^2v'}{dx'^2} = -12 \; \alpha' \int_{-1/2}^{1/2} T(x'\!,y')y'dy'$$

(2.2.8)

17

Chapter 3
Hydrostatic Model

3.1 Problem Formulation

Consider flooding the beam in Fig. 1.1 with water such that a steady layer of height h results. The steady layer, typically on the order of 1 mm, is maintained by constant replenishment of water. An energy balance on an elemental control volume of the water layer yields the following Eqn.:

$$\dot{m}''h_{fg} - \bar{h}(T_{air} - T_s) = \frac{T_h - T_s}{\dfrac{H}{k_t} + \dfrac{h}{k_w}} \qquad (3.1.1)$$

where $\dot{m}''$ is the evaporation rate, h_{fg} is the latent heat of vaporization, $\bar{h}$ is the average convective heat transfer coefficient of air across the water layer, T_{air} is the ambient air temperature, T_s is the air-water interface temperature, T_h is the hot uniform surface temperature on the bottom of the beam, k_t is the thermal conductivity of the machine tool member or beam, k_w is the thermal conductivity of the liquid water, H is the beam height, and h is the steady water layer height.

The air-water interface temperature T_s is a function of the saturation pressure of the water vapor at the interface. Fig. 3.1 is a plot of saturation temperature versus saturation pressure for water in the range $10 \leq T_s \leq 40\ °C$, along with 1st and 2nd order polynomial curve fits. As illustrated in the figure, the 2nd order polynomial is an excellent fit to the actual data. Therefore, the polynomial $P_{sat} = 5\ T^2_{sat} - 50.8\ T_{sat} + 1282.1$, where P_{sat} is in units of Pascals (Pa) and T_{sat} is in units of degrees Celcius (°C), is used to calculate the mole fractions and, hence, mass fractions of water vapor at the air-water interface. This expedites the calculation of the evaporation rate via the mass transfer driving factor.
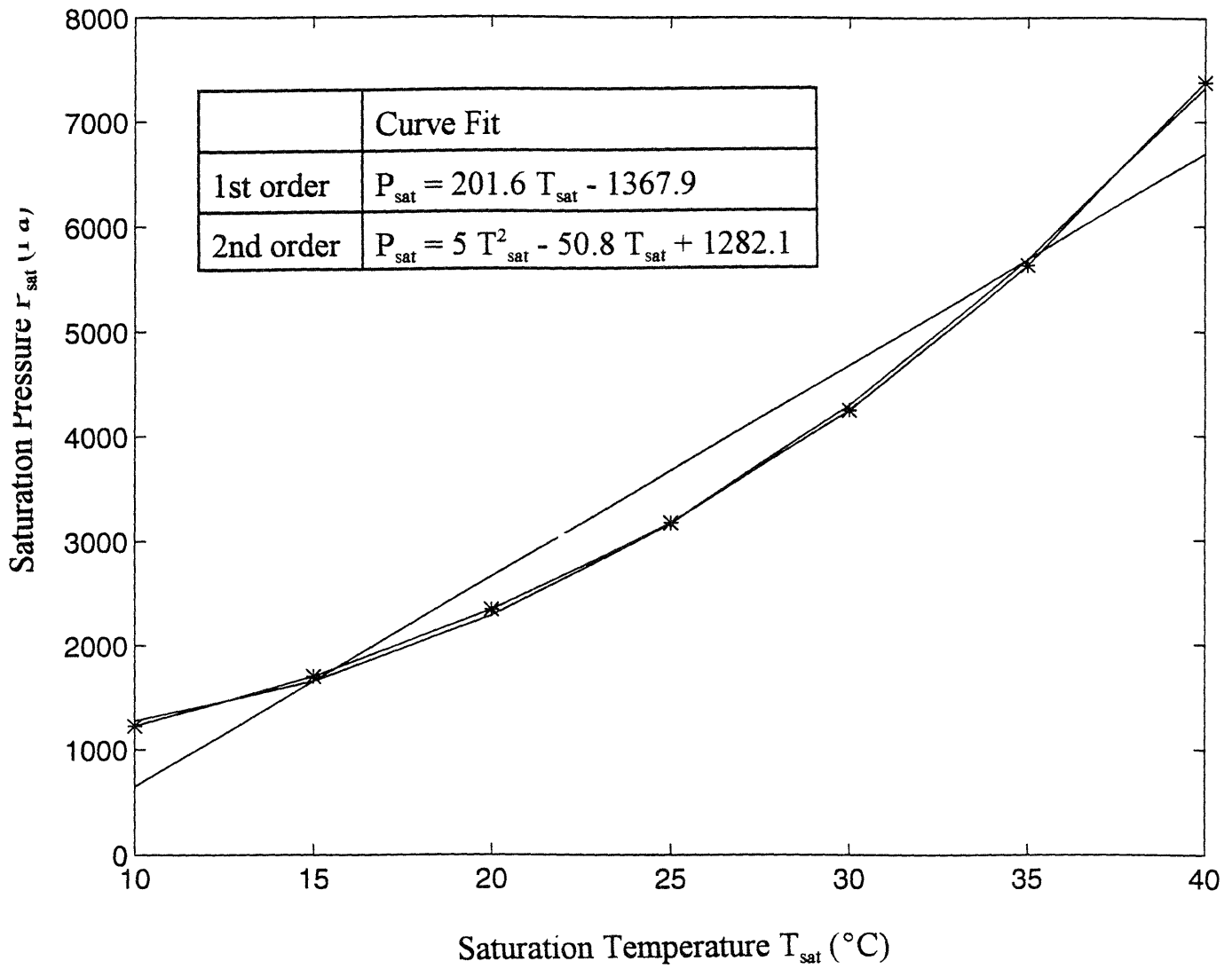
Fig. 3.1 Saturation curve for water in the range $10 \leq T_{sat} \leq 40$ °C.

3.1.1 Iterative Solution

Eqn. 3.1.1 can be solved iteratively for the air-water interface temperature T_s, after which the beam surface temperature T_c is calculated from the conductive heat flux from the beam into the water layer, given by

$$q''_{cond} = k_t \frac{(T_h - T_c)}{H} \tag{3.1.2}$$

where the conductive heat flux is calculated from the iterated value of the air-water interface temperature, expressed as

$$q''_{cond} = \frac{T_h - T_s}{\dfrac{H}{k_t} + \dfrac{h}{k_w}} \tag{3.1.3}$$

The beam thermal deflection is known to be proportional to the temperature difference across the beam. For a linear temperature variation through the beam, again referring to Fig. 2.1, given by

$$T(y) = \overline{T} - (T_h - T_c)\,(y/H) \tag{3.1.4}$$

where $\overline{T} = \dfrac{T_h + T_c}{2}$ is the average temperature in the beam. Eqn. 3.1.4 can also be expressed in terms of the dimensionless y coordinate as

$$T(y') = \overline{T} - (T_h - T_c)\, y' \tag{3.1.5}$$

20

Substituting Eqn. 3.1.5 into Eqn. 2.2.8 yields the following equation for the dimensionless distribution of thermal deflection:

$$v'(x') = \frac{\alpha'(T_h - T_c)}{2} (x')^2 \qquad (3.1.6)$$

subject to the boundary conditions $v'(x'=0) = v'(x'=L/H) = 0$. For a beam of finite length L, the maximum deflection ocurrs at x=L/2 or x'=L/2H (=Ar/2), where Ar is the beam aspect ratio L/H. This deflection is expressed as

$$\delta' = v'(x'=L/2H) = \frac{\alpha'(T_h - T_c)}{8} \left(\frac{L}{H}\right)^2 \qquad (3.1.7)$$

This result is completely consistent with the result derived by Slocum (1992, Eqn. 2.3.44, pg. 98). In fact, multiplying Eqn. 3.1.7 by the beam height H gives exactly the same dimensional result as Slocum.

3.1.2 Graphical Solution

Fig. 3.2 is a dimensionless plot of the normalized thermal deflection versus the $\alpha'\Delta T$ product for various values of the beam aspect ratio L/H. As illustrated by the plot, high aspect ratio beams are undesirable since they undergo higher thermal deflections.

Fig. 3.3 is another dimensionless plot showing the variation of the mass transfer driving factor versus a dimensionless parameter involving the relative humidity, local atmospheric pressure, and the free stream saturation pressure of water vapor at the local air temperature.

21
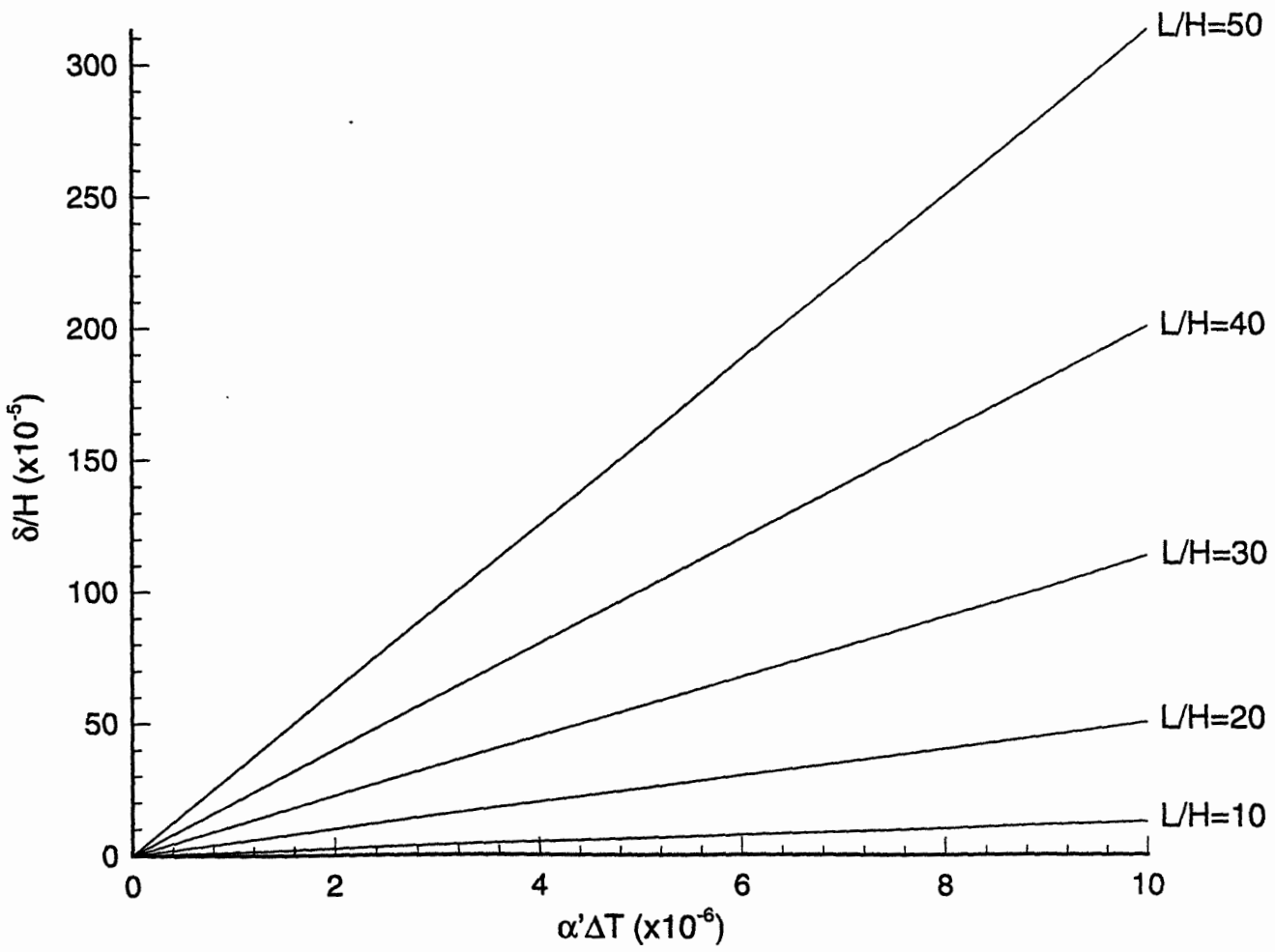
Fig. 3.2 Variation of normalized thermal deflection with the $\alpha'\Delta T$ product for selected values of the beam aspect ratio L/H.

22
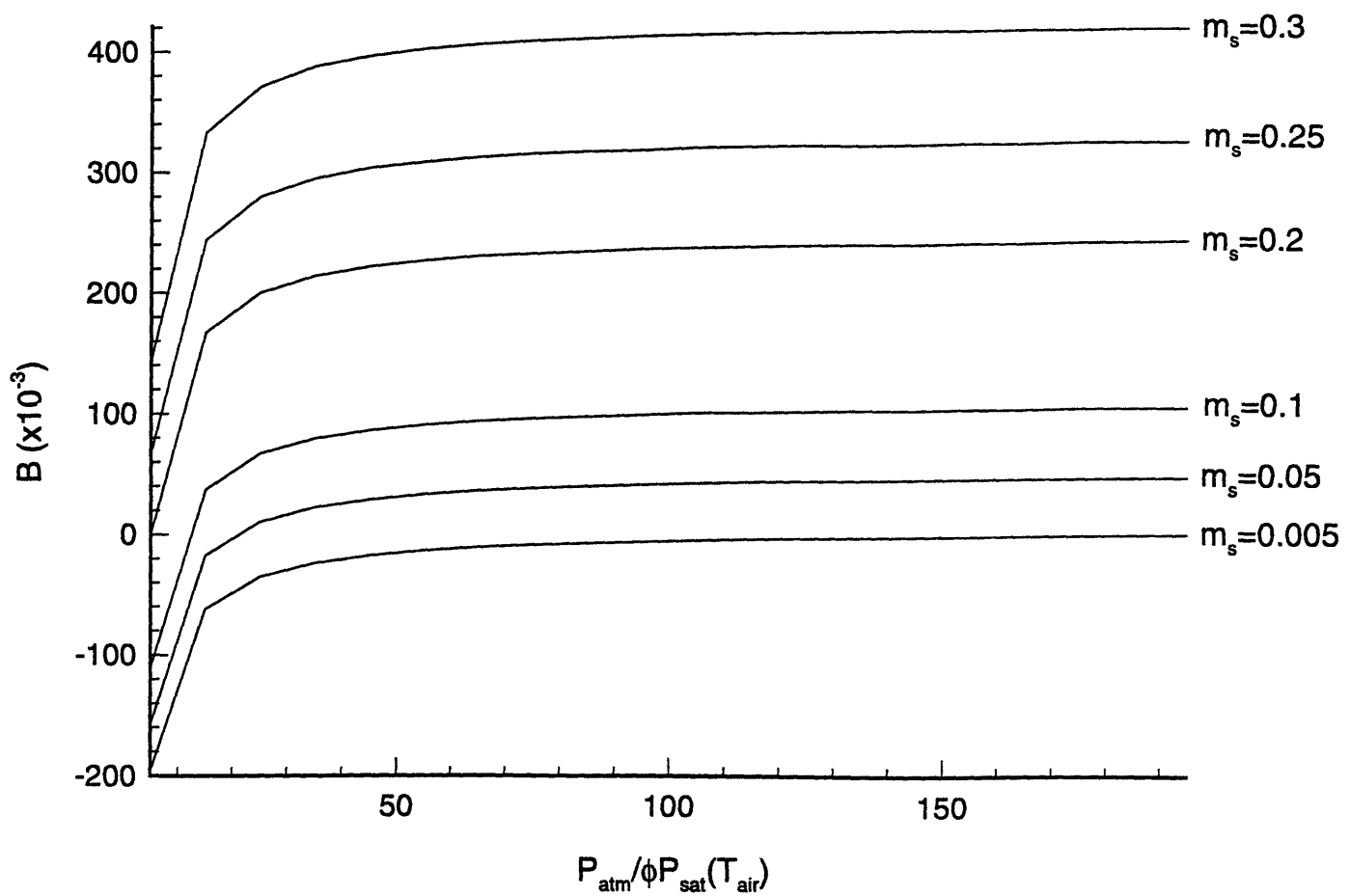
Fig. 3.3 Variation of the mass transfer driving factor with a dimensionless parameter for selected values of the mass fraction of water vapor at the air-water interface.

As shown in Fig. 3.3, the mass transfer driving factor consistently approaches an asymptotic value as the dimensionless parameter $P_{atm}/\phi P_{sat}(T_{air})$ is increased, as most of the changes in B occur for values of $P_{atm}/\phi P_{sat}(T_{air})$ less than about 50. In fact, the mass transfer driving factor approaches an asymptotic value of $B \sim \dfrac{m_s}{1 - m_s}$ for each value of the mass fraction of water vapor m_s at the air-water interface.

If we divide Eqn. 3.1.1 by $\bar{h}(T_{air} - T_s)$, we arrive at another dimensionless equation expressed as

$$\theta = \frac{T_h - T_s}{T_{air} - T_s} = Bi_{eff}(\psi - 1) \tag{3.1.8}$$

where Bi_{eff} is the effective Biot number given by

$$Bi_{eff} = \bar{h}\left(\frac{H}{k_t} + \frac{h}{k_w}\right) \tag{3.1.9}$$

and ψ is a dimensionless parameter written as

$$\psi = \frac{Le^{2/3} h_{fg} B}{c_p(T_{air} - T_s)} \tag{3.1.10}$$

Fig. 3.4 is a plot of the effective Biot number versus the dimensionless parameter ψ for select values of the dimensionless temperature difference θ.

Fig. 3.4 Variation of effective Biot number with dimensionless parameter ψ for select values of the dimensionless temperature difference θ.

25

3.1.3 Design Algorithm

In this section, a typical design algorithm is presented for a machine tool designer as follows:

1. Select the allowable thermal error or deflection for the machine tool member; extract the $\alpha'\Delta T$ product and determine the required cool-side surface temperature.

2. Now calculate the necessary air-water interface temperature.

3. With knowledge of the air-water interface temperature, calculate the mass fraction of water vapor at the air-water interface.

4. Evaluate the dimensionless parameter $P_{atm}/\phi P_{sat}(T_{air})$ and extract the mass transfer driving factor B.

5. Calculate the dimensionless temperature difference θ and the dimensionless parameter ψ; extract the effective Biot number.

6. With knowledge of the effective Biot number, calculate the required average convective heat transfer coefficient of air across the water layer and the required water layer height.

3.1.4 Illustrative Example

Usage of a combination of the iterative solution of section 3.1.2 and the design algorithm of section 3.1.3 is illustrated in this section.

Suppose the specifications of a machine tool calls for a linear carriage bearing length of 60" (1.524 m), of height 3" (0.0762 m), giving an aspect ratio of 20. The specifications also calls for a maximum thermal bending error of 10μm. This results in

$\delta/H=1.31 \times 10^{-4}$. Since the resolution of δ/H in Fig. 3.1.2 is not fine enough, Eqn. 3.1.7 is used, giving an $\alpha'\Delta T$ product of 2.62×10^{-6}. Therefore, with a beam material of granite ($\alpha'=6\mu m/m/^\circ C$), the required temperature drop across the beam is 0.436 °C. If the motor generates heat such that a uniform hot-side surface temperature of 35 °C results, the corresponding cool-side uniform surface temperature is required to be 34.564 °C. The resulting heat flux from the beam into the water layer is calculated by Eqn. 3.1.2 (with $k_t=1.6$ W/m°C for granite) to be 9.15 W/m². With a steady water layer height of 1 mm and $k_w=0.67$ W/m°C, this heat flux results in an air-water interface temperature of (Eqn. 3.1.3) 34.55 °C. Obviously, the thermal resistance of the water layer is quite small and approximately negligible. At this temperature, the saturation pressure of the water vapor at the air-water interface is (Fig. 3.1) 5.5 kPa, which results in a mole fraction (Eqn. 2.1.6) of 0.054, with the local atmospheric pressure at 101 kPa. The corresponding mass fraction of water vapor at the interface is calculated from Eqn. 2.1.4 to be 0.0343. If the local ambient air temperature in the room housing the machine tool is 15 °C (corresponding to a local saturation pressure of water vapor of 1.7 kPa) and the relative humidity is measured to be 50%, then the mole fraction of water vapor far away in the free stream is calculated by Eqn. 2.1.5 to be 0.008415. Using Eqn. 2.1.3, the mass fraction of water vapor far away in the free stream is given numerically as 0.005251, which results in a mass transfer driving factor of (Eqn. 2.1.2) 0.0301. The parameter ψ in Eqn. 3.1.10 is calculated to be 1.0036, with $h_{fg}=2440$ kJ/kg and $c_p=4.18$ kJ/kg°C for water. Eqn. 3.1.8 is used to calculate the dimensionless temperature difference. Its numerical value in this example is calculated to be 0.023, resulting in an effective Biot number of (also Eqn. 3.1.8) 6.38. Finally, Eqn. 3.1.9 requires the maximum average convective heat transfer coefficient of air across the water layer to be 129.89 W/m² °C. This can be achieved simply by carefully blowing air across the machine tool.

Chapter 4

Hydrodynamic Model

4.1 Problem Formulation

Again, consider the beam in Fig. 1.1, of length L and height H, subject to a hot-side uniform surface temperature of T_h, uniform water flow across the cool-side surface at flow rate $\dot{m}$ with steady layer height h and inlet temperature T_h, and no heat loss (adiabatic) from either end of the beam. The local ambient air temperature is T_{air}, with relative humidity ϕ. In addition, air flows across the water layer such that an average convective heat transfer coefficient $\bar{h}$ results. The local pressure in the room housing the machine tool is P_{atm}.

4.2 1-D Analytic Model and Solution

In the steady-state 1-D analytic model, it is assumed that there is no axial variation in the conductive heat flux from the beam into the water layer. As such, there exists a linear variation of temperature through the beam at any axial location. On the cool-side of the beam, with water flow, one must account for change in enthalpy of the water as it flows along the beam in the axial direction. This, along with the effects of convective cooling and evaporative cooling, causes a temperature drop along the beam in the axial direction. Again, considering an energy balance on an elemental control volume of the water layer, the ordinary differential equation governing the temperature of the air-water interface is derived as

$$\dot{m}c_p \frac{dT_s}{dx} + \frac{P}{R_{cond}}(T_s - T_h) + \frac{P}{R_{conv}}(T_s - T_{air}) + P\dot{m}''h_{fg} = 0 \qquad (4.2.1)$$

where P is the surface heat transfer perimeter, T_s is the temperature of the air-water interface, R_{cond} is the conduction resistance of the beam and water layer, and R_{conv} is the convective resistance of the air flow across the water layer. These resistances are defined as

$$R_{cond} = \frac{H}{k_t} + \frac{h}{k_w} \qquad (4.2.2)$$

$$R_{conv} = \frac{1}{\bar{h}} \qquad (4.2.3)$$

In Eqn. 4.2.1, T_s is taken approximately as the bulk fluid temperature T_{bulk} and the 2nd term on the righ-hand side of Eqn. 4.2.2 is essentially negligible. Note that all other variables in Eqn. 4.2.1 have been defined previously. In addition, the water mass flow rate $\dot{m}$, specific heat c_p, and latent heat of vaporization h_{fg} are all assumed constant. In Eqn. 4.2.1, the 1st term represents the net change in enthalpy through the control volume element. The 2nd and 3rd terms represent heat conduction into the water layer and convective heat loss from the water layer, respectively. The last term represents evaporative cooling.

Assuming the low rate approximation to be valid, Eqn. 2.1.9 represents the evaporation rate $\dot{m}''$ of the water and Eqns. 2.1.2-2.1.6 and Eqn. 2.1.10 remains valid. If the mass fraction of water vapor at the air-water interface m_s is much less than unity, then Eqn. 2.1.2 reduces to

$$B_i = m_{i,s} - m_{i,e} \qquad (4.2.4)$$

Eqn. 2.1.3 remains unchanged under this assumption; however, in Eqn. 2.1.4, this assumption implies that the mole fraction of water vapor at the air-water interface $X_{h_2o,s}$ is also much less than unity since the molecular weights of air and water are not greatly different. This in turn implies that the saturation pressure of water vapor at the air-water interface temperature $P_{sat}(T_s)$ is much less than the local atmospheric pressure P_{atm}. As a result, Eqn. 2.1.4 reduces to

$$ m_{i,s} \approx \left(\frac{M_{h_2o}}{M_{air}} \right) \left(\frac{P_{sat}(T_s)}{P_{atm}} \right) \tag{4.2.5} $$

where

$$ P_{sat}(T_s) \approx 5\ T_s^2 - 50.8\ T_s + 1282.1 \tag{4.2.6} $$

Note that Eqn. 4.2.6 is a valid approximation since, in the range $10 \le T_{sat} \le 40\ °C$, the air-water interface temperature (T_s) is equivalent to the saturation temperature (T_{sat}) of water vapor at the air-water interface. The units of T_s and P_{sat} are $°C$ and Pa, respectively. Substituting Eqns. 4.2.4-4.2.6 into Eqn. 4.2.1 results in the following nonlinear differential equation for the air-water interface temperature:

$$ \frac{dT_s}{dx} = q_2\ T_s^2 + q_1\ T_s + q_0 \tag{4.2.7} $$

where

$$q_2 = -\frac{5Ph_{fg}g \, {}^*M_{h_2o}}{\dot{m}c_p M_{air} P_{atm}} \qquad (4.2.8)$$

$$q_1 = -\frac{P}{\dot{m}c_p}\left[\frac{1}{R_{cond}} + \frac{1}{R_{conv}} - \frac{50.8h_{fg}g \, {}^*M_{h_2o}}{M_{air} P_{atm}}\right] \qquad (4.2.9)$$

$$q_0 = \frac{P}{\dot{m}c_p}\left[\frac{T_h}{R_{cond}} + \frac{T_{air}}{R_{conv}} + h_{fg}g \, {}^*\left(m_{i,s} - \frac{1282.1M_{h_2o}}{M_{air} P_{atm}}\right)\right] \qquad (4.2.10)$$

Eqn. 4.2.7 is known in the literature as Ricatti's equation, which, fortunately, lends itself to an analytic solution technique.

The solution to Ricatti's Equation is such that if one solution $T_s = T_s{}^*$ is known, then by making the change of variable $T_s = T_s{}^* - c_1 / u$ with c_1 an arbitrary constant, Eqn. 4.2.7 is transformed to

$$\frac{du}{dx} + (q_1 + 2q_2 T_s{}^*)u = c_1 q_2 \qquad (4.2.11)$$

which is a 1st order linear differential equation. Since q_2, q_1, and q_0 are all constants, a solution that satifies Eqn. 4.2.7 is a constant solution found by setting the right-hand side of Eqn. 4.2.7 to zero as follows:

$$q_2 T_s{}^{*2} + q_1 T_s{}^* + q_0 = 0 \qquad (4.2.12)$$

The solution to this quadratic equation is

31

$$T_s* = -\frac{q_1}{2q_2} \pm \sqrt{\left(\frac{q_1}{2q_2}\right)^2 - \left(\frac{q_0}{q_2}\right)} \qquad (4.2.13)$$

Now, with one known solution T_s*, Eqn. 4.2.11 is solved by multiplying by the integrating factor $e^{\beta x}$, where $\beta = q_1 + 2q_2T_s*$, and integrating to get the general solution, expressed as

$$u = \frac{c_1 q_2}{\beta} + c_2 e^{-\beta x} \qquad (4.2.14)$$

where c_2 is a constant. Substituting Eqn. 4.2.14 into the equation for the change of variable, the general solution to Eqn. 4.2.7 is given by

$$T_s = T_s* - \frac{1}{\dfrac{q_2}{\beta} + ce^{-\beta x}} \qquad (4.2.15)$$

where $c = c_2 / c_1$ is a constant to be determined from application of the boundary condition. The appropriate boundary condition is $T_s (x=0) = T_h$. Therefore, the particular solution to Eqn. 4.2.7 is

$$T_s(x) = T_s* - \frac{1}{\dfrac{q_2}{\beta} + \zeta e^{-\beta x}} \qquad (4.2.16)$$

where

$$\zeta = \frac{1}{T_s* - T_h} - \frac{q_2}{\beta} \qquad (4.2.17)$$

32

Eqn. 4.2.16 is the temperature distribution of the air-water interface. Recall that since the steady water layer height h is small (on the order of a millimeter), the thermal resistance of the water layer can be neglected and the approximation $T_c \cong T_s$ can be made, where T_c is the temperature distribution of the cool-side surface of the machine tool.

The distribution of thermal deflection is calculated by performing the integration in Eqn. 2.2.8 and subsequently integrating as follows:

$$\delta'(x') = \alpha' \int\limits_{0}^{x'} \left(\int\limits_{0}^{t'} \Delta T(s') ds' \right) dt' \qquad (4.2.18)$$

where $\Delta T = T_h - T_c$ is the temperature difference across the beam, which varies axially. The boundary conditions are taken as $\delta'(x'=0) = \dfrac{d\delta'}{dx'}(x'=0) = 0$ Eqn. 4.2.18 is solved by first plotting $\Delta T(s')$ versus s' and fitting a curve through it, then performing the integrations accordingly.

It turns out that the distribution of temperature on the cool-side surface of the beam can be very closely approximated by a 3rd order polynomial, expressed as

$$T_s(x') = a (x')^3 + b (x')^2 + c (x') + d' \qquad (4.2.19)$$

where a,b,c,and d' are all constants determined from the curve fit of the plot of $T_s(x')$ versus x'. The polynomial approximation of the temperature difference across the beam is given by

$$\Delta T(x') = -a (x')^3 - b (x')^2 - c (x') + d \qquad (4.2.20)$$

33

where $\Delta T(x')$ is defined as $\Delta T(x') = T_h - T_s(x')$ and $d = T_h - d'$.

Figs. 4.1-4.5 are comparisons of the iterative and low-rate approximate solutions for the air-water interface temperature for the static case with $\bar{h} = 5$ $W/m^2\,°C$ and several hot-side surface and ambient air temperatures as a function of relative humidity.

The low-rate approximation is an overestimation of the air-water interface temperature since the evaporation rate is effectly suppressed. This overestimation can lead to significant errors in the calculation of the thermal deflection, which is unacceptable for precision machine tool applications. In fact, thermal deflections are underestimated since, as shown in Figs. 4.1-4.5, the iterative solutions consistently result in lower air-water interface temperatures, which leads to higher thermal deflections. Therefore, the errors shown in Figs. 4.1-4.5 should be used to correct the low-rate approximate solutions and, subsequently, increase the accuracy in the calculation of the thermal deflections.

For the hydrodynamic case, it is assumed that other dynamic effects are effectively dominant and the effects of the low-rate approximation are essentially miniscule. This is especially true at higher water mass flow rates.
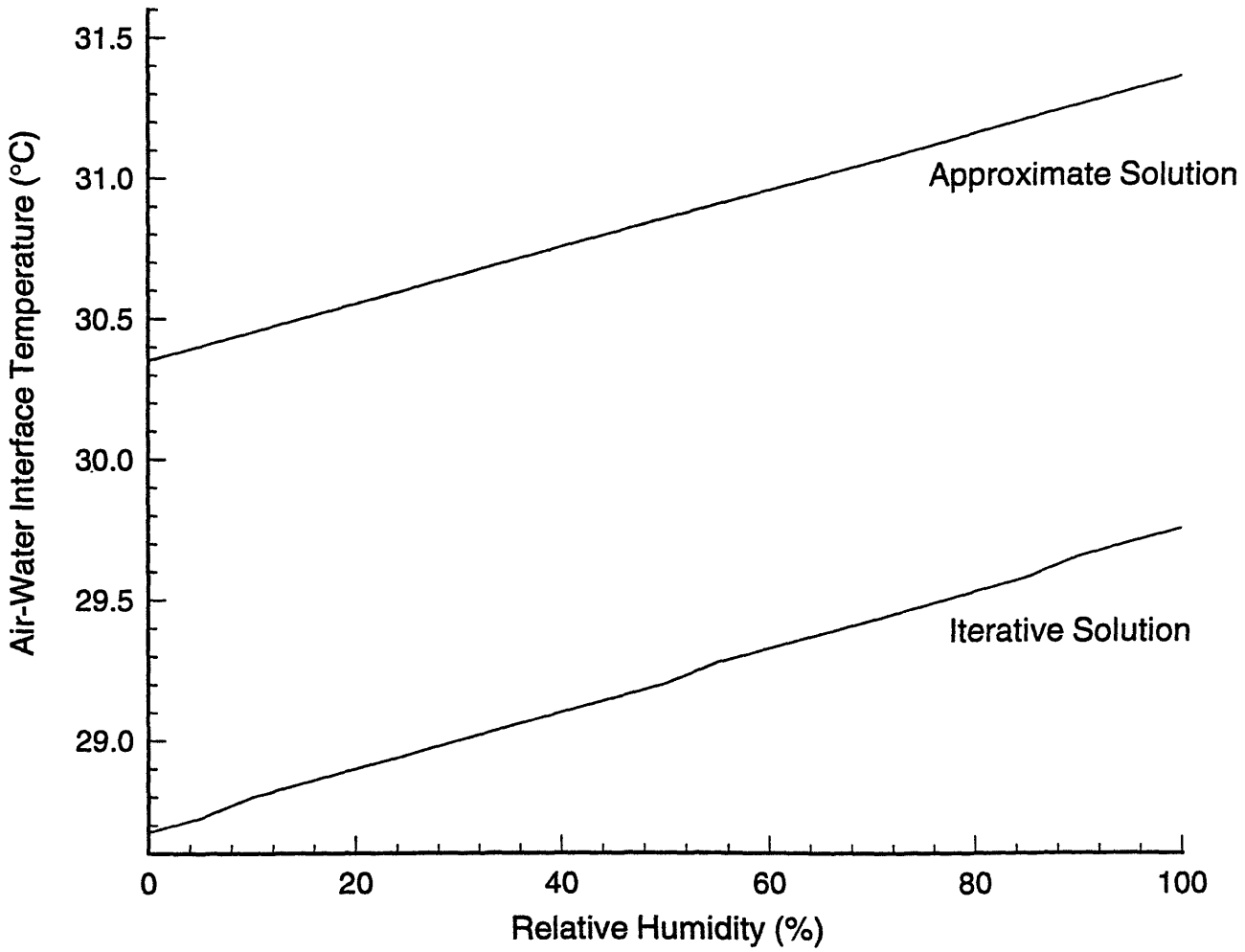
Fig. 4.1 Comparison of the iterative solution and low-rate approximate solution for the air-water interface temperature as a function of relative humidity (static case).
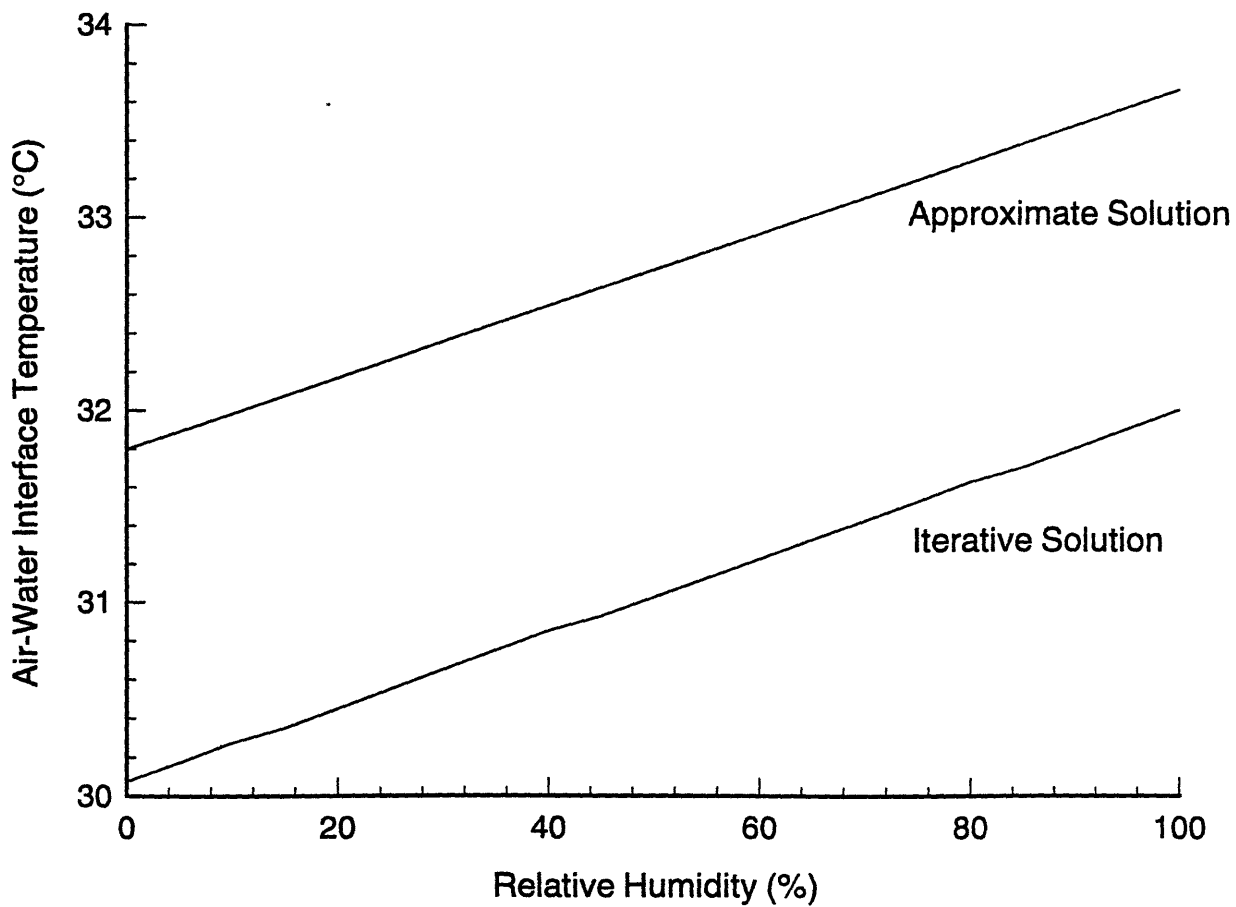
T_h=35 °C and T_{air}=25 °C

Fig. 4.2 Comparison of the iterative solution and low-rate approximate solution for the air-water interface temperature as a function of relative humidity resulting from a higher ambient air temperature (static case).
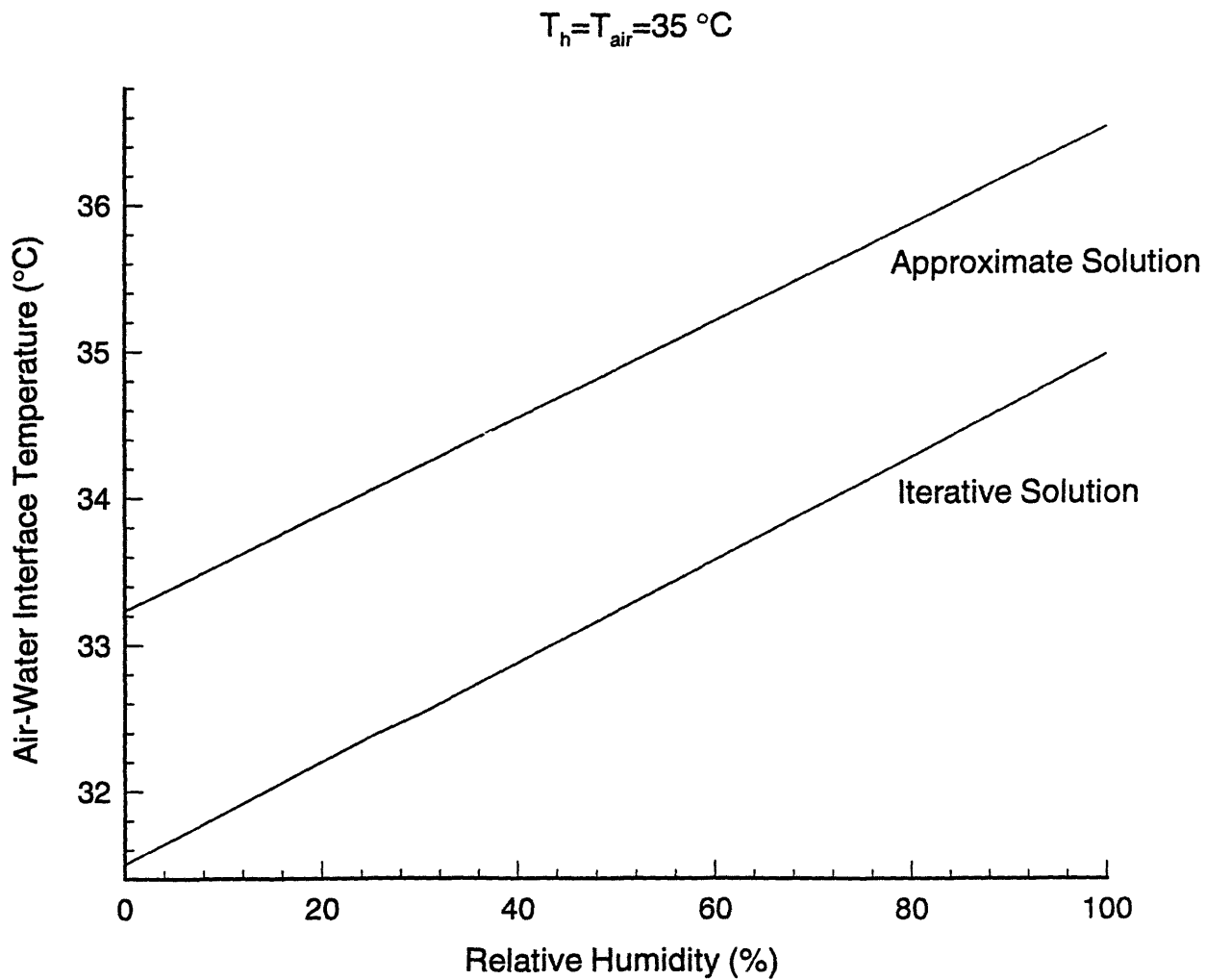
36

$T_h=T_{air}=35\ ^\circ C$

Fig. 4.3 Comparison of the iterative solution and low-rate approximate solution for the air-water interface temperature as a function of relative humidity resulting from equivalent hot-side surface and ambient air temperatures (static case).

Fig. 4.4 Comparison of the iterative solution and low-rate approximate solution for the air-water interface temperature as a function of relative humidity resulting from a lower hot-side surface temperature (static case).
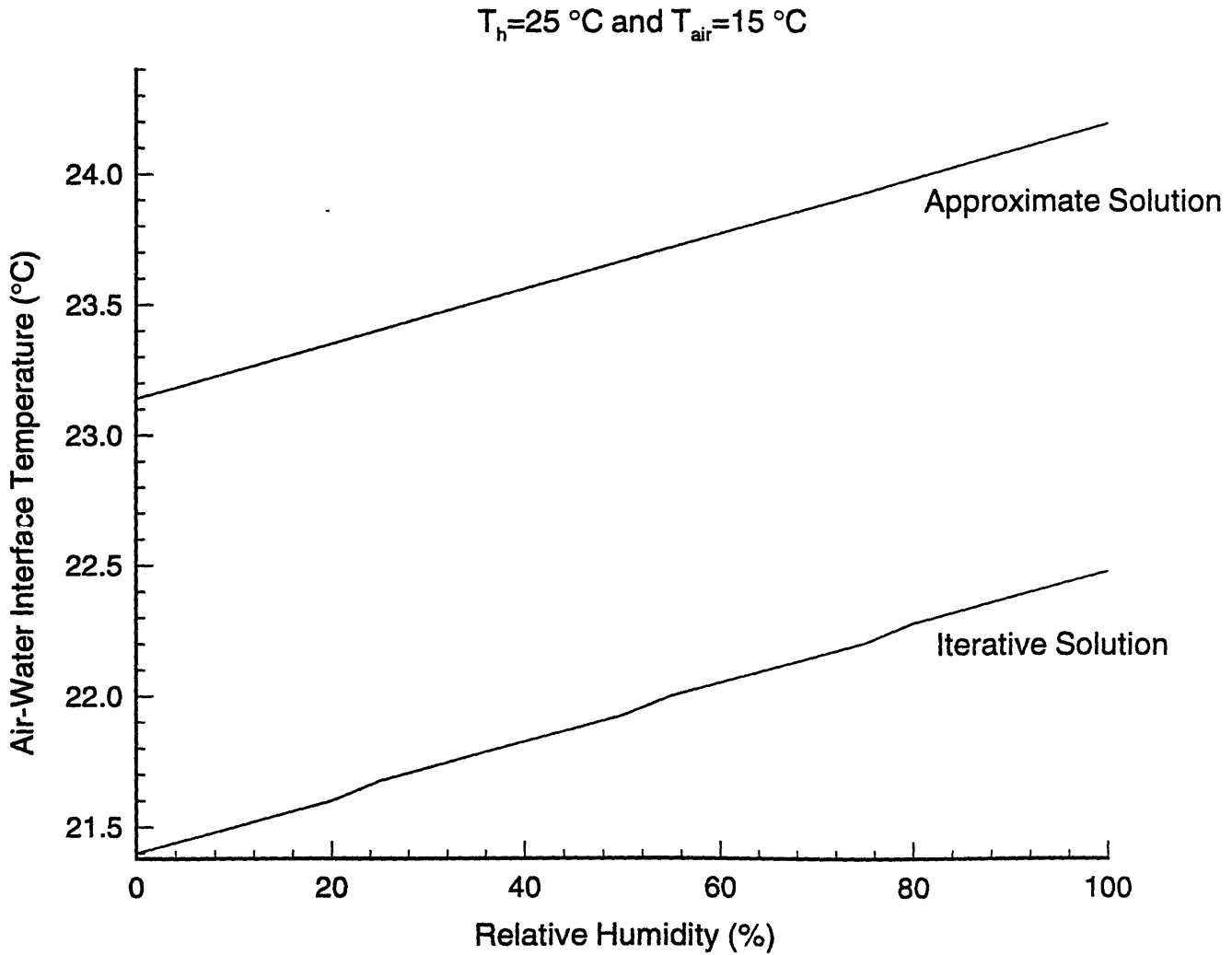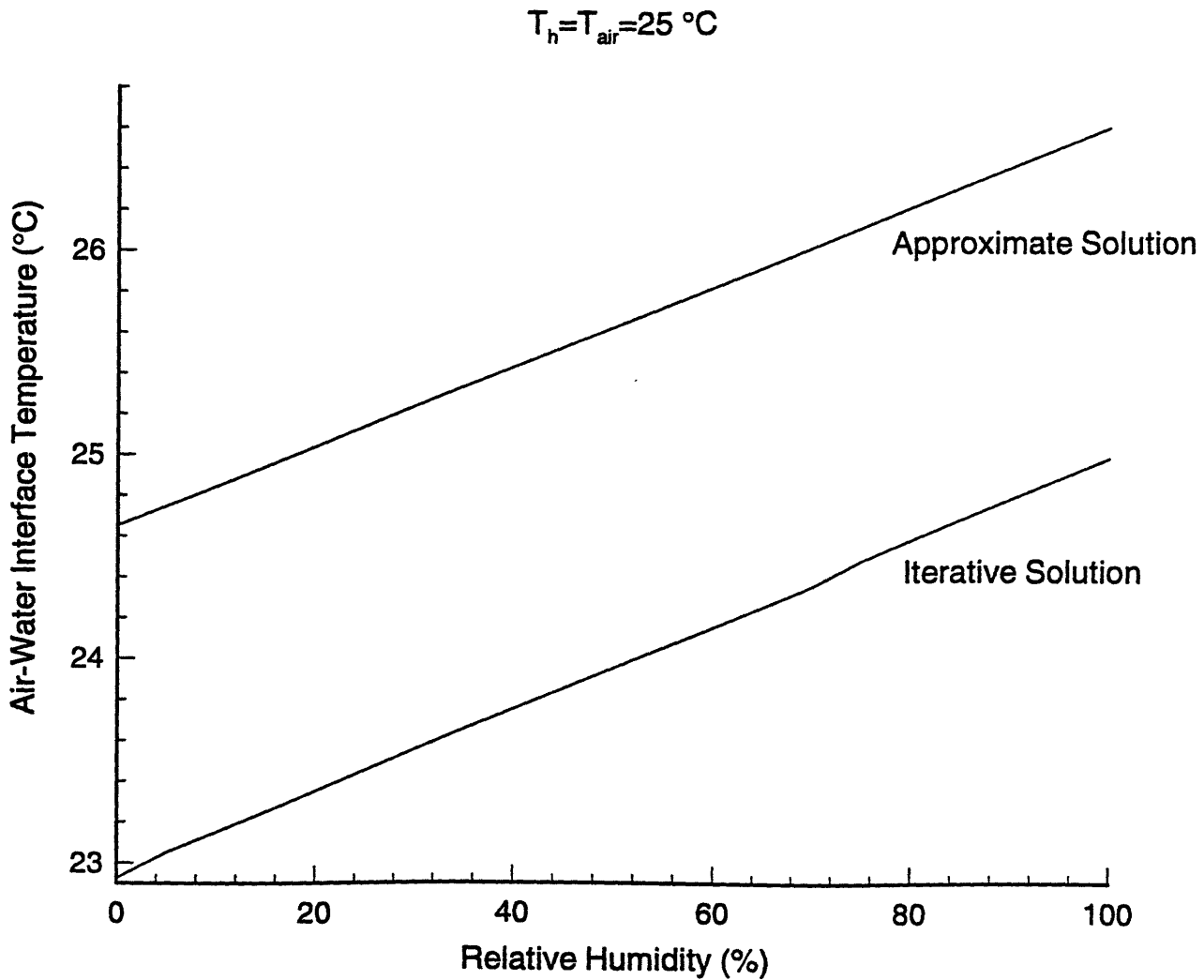
Fig. 4.5 Comparison of the iterative solution and low-rate approximate solution for the air-water interface temperature as a function of relative humidity resulting from equivalent lower hot-side surface and ambient air temperatures (static case).

Table 4.1 is a comparison of the extremal relative errors corresponding to the solutions illustrated in Figs. 4.1-4.5. The minimum and maximum errors occur at 100 and 0 percent relative humidity, respectively.

T_h (°C)	T_{air} (°C)	Relative Error (%)	
		Minimum	Maximum
35	15	5.40	5.85
35	25	5.19	5.73
35	35	4.46	5.50
25	15	7.63	8.13
25	25	6.49	7.53

Table 4.1 Comparison of extremal relative errors in the iterative and low-rate approximate solutions for the air-water interface temperature.

In what follows, an example of the utility of Eqn. 4.2.16 and Eqns. 4.2.18-4.2.20 is illustrated graphically. Fig. 4.6 is a plot of the distribution of temperature and thermal deflection of a machine tool member, of length 1.37 m and height 0.0635 m, subject to evaporative cooling. A unit perimeter is assumed and the thermal expansion coefficient is taken as 6 μm/m°C for granite. The dimensions and thermal properties used are taken from specifications of the Hydroguide™ self-compensating hydrostatic water bearing. The effect of variation of the average convective heat transfer coefficient is also shown. As one can see, an increase in the heat transfer coefficient significantly lowers the surface temperature and increases the thermal deflection. Note that the minimum temperature and maximum thermal deflection ocurrs at the right side of the beam where the water exits. In fact, the lower average convective heat transfer coefficient yields a smaller end deflection of approximately 152 microns. In Fig. 4.7, the ambient air temperature is increased to

25 °C, which results in (not suprisingly) smaller variations of temperature and thermal deflection along the beam. Again, the lower average convective heat transfer coefficient results in a smaller end deflection of about 127 microns. Fig. 4.8 shows the effect of increasing the flow rate of water across the beam. As one would expect, increasing the water flow rate tends to drive the beam isothermal. This happens because the residence time of the water flowing along the beam is smaller at higher flow rates, which means that there's not enough time for the convective and evaporative cooling processes to take place. Of course, an isothermal beam results in no thermal deflection since the deflection is proportional to the temperature difference across the beam. However, at 80 g/s, the smallest end deflection is approximately 25 microns. Lastly, Fig. 4.9 illustrates that convective and evaporative cooling takes place even when the ambient air temperature and hot-side beam temperature are equal. As noted before, increasing the water flow rate tends to drive the beam to an isothermal state. In this case, the smallest end deflection of about 12 microns occurs at 80 g/s.
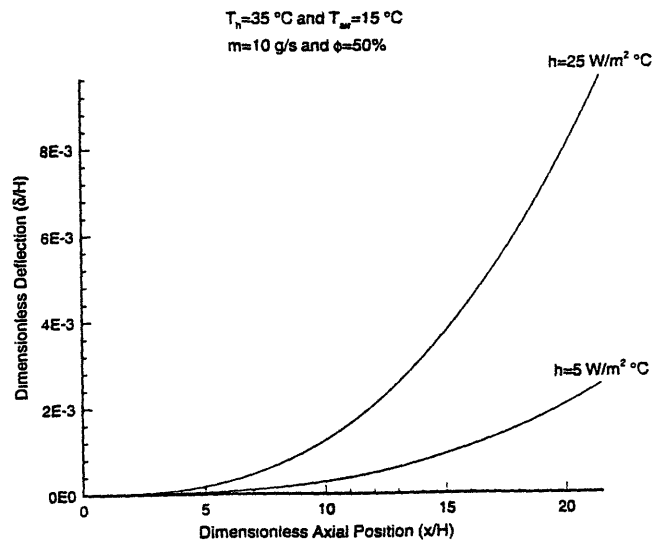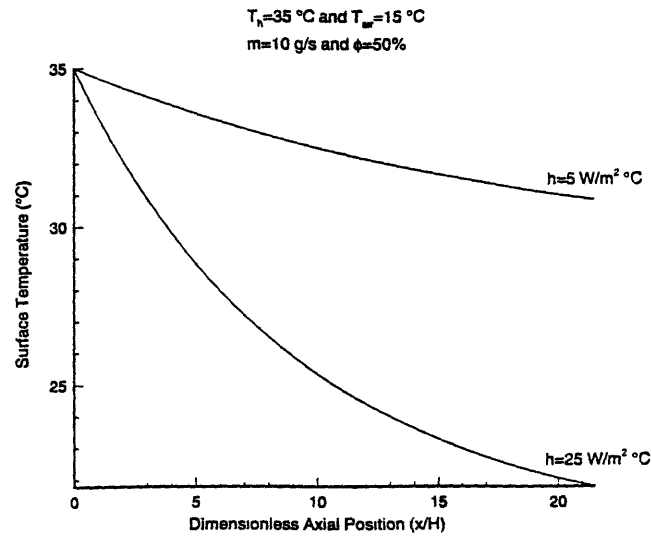
Fig. 4.6 Distribution of cool-side surface temperature and beam thermal deflection as a function of average convective heat transfer coefficient (1-D).
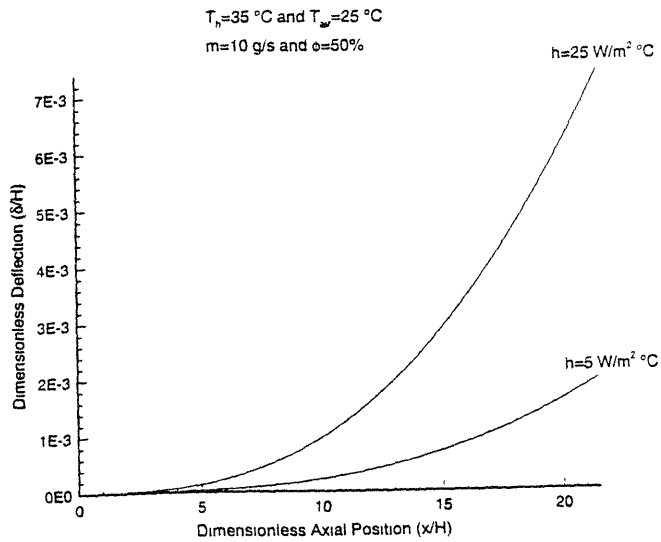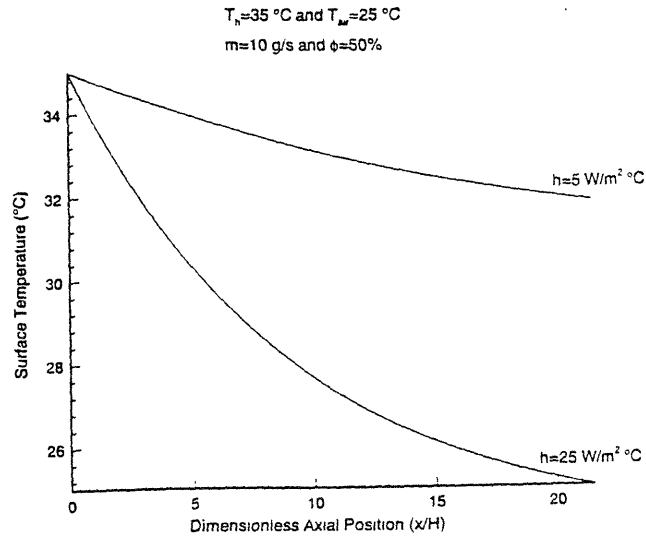
42

Fig. 4.7 Distribution of cool-side surface temperature and beam thermal deflection as a result of an increase in the ambient temperature (1-D).
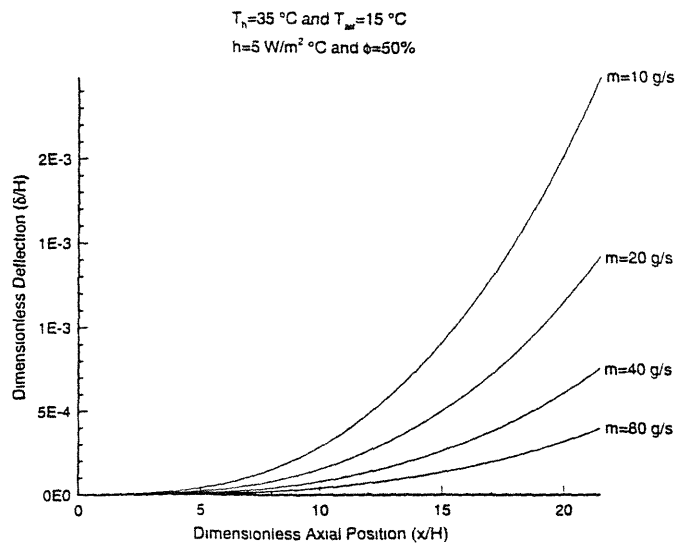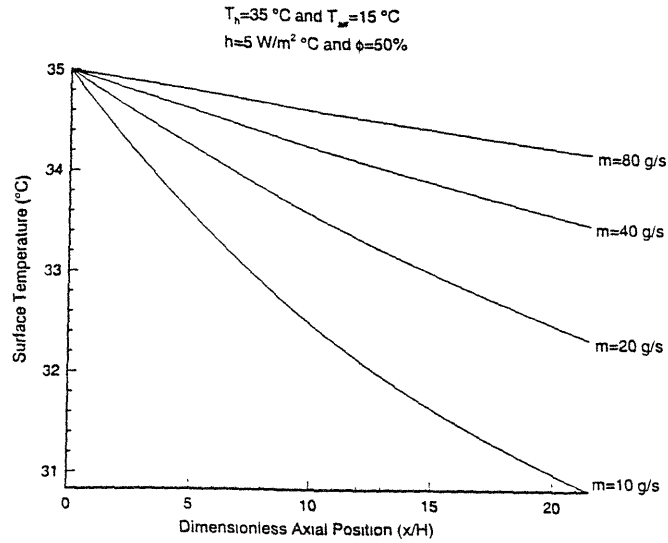
43

Fig. 4.8 Distribution of cool-side surface temperature and beam thermal deflection as a function of water mass flow rate (1-D).
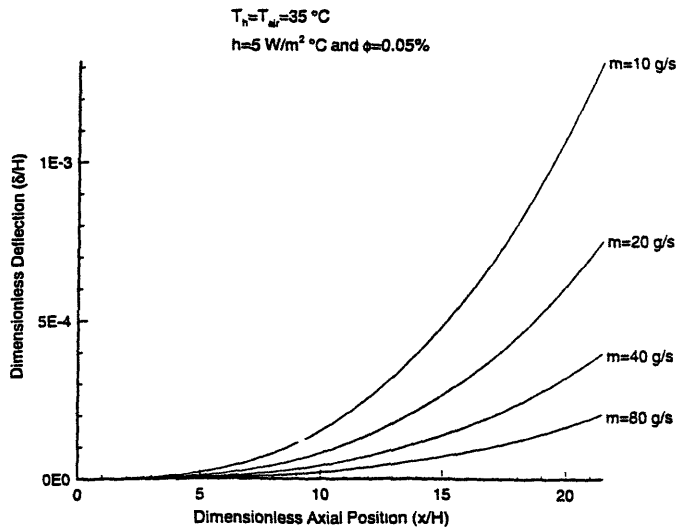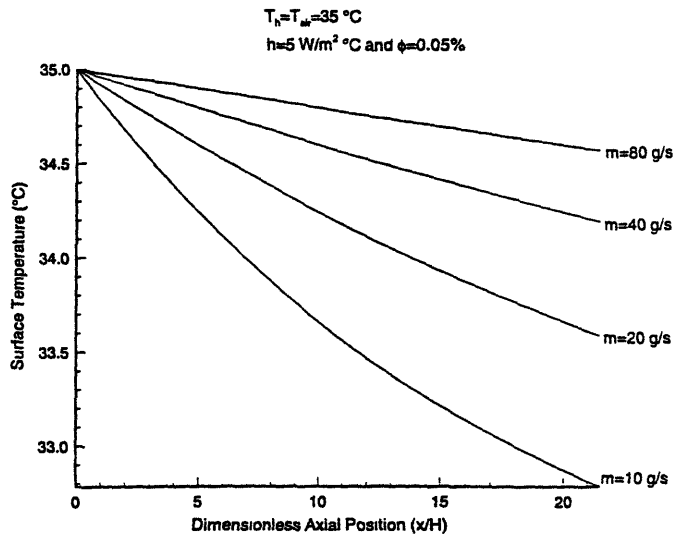
Fig. 4.9 Distribution of cool-side surface temperature and beam thermal deflection as a function of water mass flow rate when the hot-side surface temperature and the ambient air temperature are equal (1-D).

4.3 2-D Numerical Model

As the water flows along the beam, the mechanisms of convective cooling and evaporative cooling causes a temperature drop in that direction. This temperature variation causes an axial gradient in the conductive heat flux from the beam into the water layer. This axial gradient must be taken into account when solving for the temperature distribution of the air-water interface (Ricatti's equation). This essentially couples the solution for the temperature distribution in the beam to the temperature distribution of the air-water interface. In the 1-D model, they were completely decoupled.

4.3.1 Discretization of the Governing Equations

The equation governing 2-D, steady-state, constant property heat conduction in the beam in the absence of sinks or sources is Laplace's equation given by

$$\frac{\partial^2 T}{\partial x^2} + \frac{\partial^2 T}{\partial y^2} = 0 \qquad (4.3.1)$$

Consider the 2-D control volume shown in Fig. 4.10 (Patankar, 1980). The derivatives in Eqn. 4.3.1 are approximated by 3-point central differences as follows:

$$\frac{\partial^2 T}{\partial x^2} \sim \frac{T_E - 2T_P + T_W}{(\Delta x)^2} \qquad (4.3.2)$$

$$\frac{\partial^2 T}{\partial y^2} \sim \frac{T_N - 2T_P + T_S}{(\Delta y)^2} \qquad (4.3.3)$$

Upon substituting Eqns. 4.3.2 and 4.3.3 into Eqn. 4.3.1, the discretization equation for the temperature distribution in the beam is derived as follows:

$$a_P T_P = a_E T_E + a_W T_W + a_N T_N + a_S T_S \qquad . \qquad (4.3.4)$$

where $a_E = a_W = \Delta y \, / \, \Delta x$, $a_N = a_S = \Delta x \, / \, \Delta y$, and $a_P = a_E + a_W + a_N + a_S$.
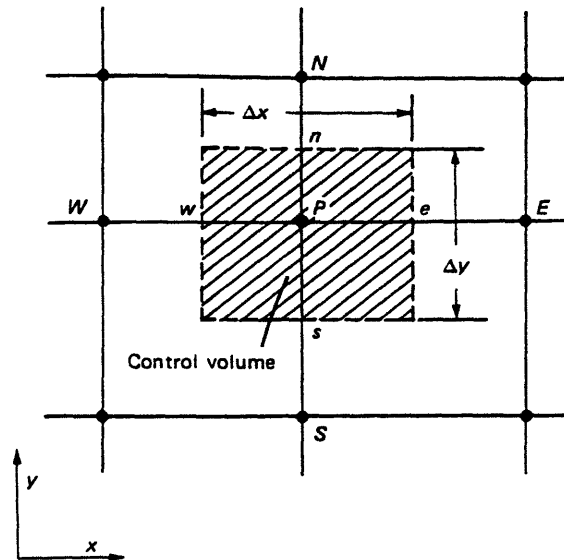

Fig. 4.10 Typical cell in the discretized domain of the 2-D model (from Patankar, 1980).

For the 2-D model, Eqn. 4.2.1 is modified to account for the axial variation in the conductive heat flux from the beam into the water layer as follows:

$$\dot{m}c_p \frac{dT_s}{dx} + P\bar{h}(T_s - T_{air}) + Pk_t \left[\frac{\partial T}{\partial y} \right]_{y=H} + P\dot{m}''h_{fg} = 0 \qquad (4.3.5)$$

47

where the evaporation rate $\dot{m}''$ is approximated as in the 1-D model as

$$\dot{m}'' \approx g^* \left[\frac{M_{h_2o}}{M_{air}P_{atm}} (5T_s^2 - 50.8T_s + 1282.1) - m_{i,s} \right] \qquad (4.3.6)$$

The derivative in the 1st term in Eqn. 4.3.5 is approximated by a two-point central difference scheme whereas the derivative in the 3rd term in Eqn. 4.3.5 is approximated by a two-point forward difference scheme.

As in the 1-D model, temperature variations through the water layer are neglected since the water layer thermal resistance is negligibly small. As such, the temperature distribution of the air-water interface is approximately equal to the temperature distribution of the cool-side surface of the beam. Upon substituting Eqn. 4.3.6 into Eqn. 4.3.5 with the appropriate difference approximations, the discretized form of Eqn. 4.3.5 is written in quadratic form as

$$a T_p^2 + b T_p + c = 0 \qquad (4.3.7)$$

where $a = 5Ph_{fg}g^*\psi$, $b = Ph - 50.8\ Ph_{fg}g^*\psi + Pk_t/\Delta y$, and $c = (mc_p T_E - mc_p T_W)/2\Delta x$ $+ PhT_{air} + Ph_{fg}g^*(1282.1\psi - m_{i,e}) - Pk_t T_S/\Delta y$, where $\psi = M_{h2o}/(M_{air}P_{atm})$. Of course there are two solutions that satisfy Eqn. 4.3.7; however, a trial and error process reveals that the only physically realizable solution is

$$T_p = -\frac{b}{2a} + \sqrt{\left(\frac{b}{2a}\right)^2 - \frac{c}{a}} \qquad (4.3.8)$$

Note that Eqn. 4.3.8 only applies to the nodes on the cool-side surface of the beam in the discretized domain whereas Eqn. 4.3.4 applies only to the interior nodes of the beam. On the adiabatic boundaries at x=0 and x=L we impose the condition $T_W=T_P$ and $T_E=T_P$, respectively, for all y. Of course, on the hot-side surface of the beam we require that $T_P=T_h$, for all x.

The distribution of thermal deflection is calculated as in section 4.2, where in Eqn. 4.2.18, $\Delta T(s')$ is replaced by

$$ f_P = -12 \; \alpha \int\limits_{-1/2}^{1/2} T(x'_P, y') y' dy' \qquad (4.3.9) $$

The integral in Eqn. 4.3.9 is calculated using the Composite Simpson's Rule found in Maron (1987, pg. 353). Also, as in section 4.2, the distribution of f_p is approximated by a 3rd order polynomial and the integrations carried out accordingly.

4.3.2 Solution Algorithm

The numerical solution of the discretized equations of section 4.3.1 is carried out using the Gauss-Seidel iterative scheme with relaxation. The relaxation parameter ω, in the range $0 < \omega < 2$, allows for rapid convergence of the iterative scheme. The iterative scheme, with relaxation, is carried out with the following equation:

$$ T^{i+1} = T^i + \omega(T_P - T^i) \qquad (4.3.10) $$

where with $\omega=1$ the scheme reduces to the Gauss-Seidel iterative scheme. In Eqn. 4.3.10, T_P is given by Eqn. 4.3.4, after dividing by a_P of course. Generally, there is an optimal value for ω, which depends on the particular problem under study. However, in the

49

present study, an optimal value is not sought, and underrelaxation (ω < 1) is used to achieve convergence. Convergence is achieved when the absolute difference between T^{i+1} and T^i in Eqn. 4.3.10 is less than or equal to some pre-established criterion. This criterion is specified in section 4.3.3.

The following is the algorithm used to solve the discretized equations by the iterative scheme:

1. Specify constants including imposed boundary conditions.

2. Provide initial guess values for the solution vector (temperature in this case).

3. Calculate new solution vector and compare with solution vector from previous iteration.

4. If the difference in step 3 is less than or equal to some pre-established convergence criterion for all components of the solution vector, then output the converged solution vector. Otherwise, set the new unconverged solution vector equal to the initial guess solution vector and repeat step 3 until a converged solution vector is reached.

4.3.3 Convergence Criteria and Grid Independency

The chosen convergence criterion in the iterative solution for the nodal temperatures is $\varepsilon = 10^{-5}$. The convergence criterion is such that the variation in the nodal temperatures are less than or equal to ε from one iteration to the next for all nodes.

Grid independency occurs when changing the grid size produces no significant difference in the solution for the nodal temperatures. The average temperature of the cool-side surface is used to establish grid independency. Grid independency is established when the variation of the average temperature of the cool-side surface is less than 5%

when varying the grid size. The average temperature is calculated using the Composite Simpson's Rule of Maron (1987, pg. 353).

In the present study, a grid size of 87x29 was found to establish grid independent results. However, a grid size of 105x35 was used to ensure increased accuracy in the solution for the nodal temperatures.

4.3.4 Numerical Results

The numerical results contained in this section are presented based on the Hydroguide^{TM} dimensions and thermophysical properties. They are reiterated as follows:

$$L = 1.37 \text{ m}$$
$$H = 0.0635 \text{ m}$$
$$P = 1 \text{ m}$$
$$\alpha' = 6 \ \mu\text{m/m} \ ^\circ\text{C}$$
$$k_t = 1.6 \text{ W/m} \ ^\circ\text{C}$$
$$c_p = 4.18 \text{ kJ/kg} \ ^\circ\text{C}$$
$$h_{fg} = 2.44 \text{ MJ/kg}$$

The resulting fixed beam aspect ratio is $L/H = 21.57$ and the thermophysical properties are taken at $20\,^\circ\text{C}$, which do not vary significantly over the temperature ranges encountered in this study.

A note regarding the adiabatic assumption is warranted. The adiabatic assumption essentially places a lower bound on the thermal deflection (at the liquid supply end) since any heat loss from the ends would effectively lead to higher temperature drops through the beam. In a practical sense, a beam made adiabatic on its ends would result in lower thermal deflections than a beam made perfectly conducting at its ends.

Fig. 4.11 is a plot of the distribution of cool-side surface temperature and thermal deflection as a function of water mass flow rate. As expected, increasing the flow rate tends to drive the beam to an isothermal state, which results in minimal thermal deflection.

Note that the maximum deflection occurs at the right end of the beam where the water exits. The smallest end deflection is estimated to be about 23 microns, which occurs at 80 g/s. Fig. 4.12 illustrates the distribution of isotherms as a function of water mass flow rate. In each case, the isotherm distribution is approximately 0.3 °C/isotherm with uniform hot-side surface temperature T_h distributed on the bottom of the beam. Note also the two-dimensional nature of the heat flow as the water flow rate is increased and the one-dimensional nature of the heat flow in the static case. However, in the flow case, as the water travels "downstream" of the beam entrance, a transition occurs whereby 2-D effects are essentially negligible. Fig. 4.13 shows the effect of varying the average convective heat transfer coefficient. As expected, an increase in the average convective heat transfer coefficient tends to drive the cool-side surface temperature closer to the ambient air temperature, which leads to higher thermal deflections. According to this figure, the smallest end deflection is approximately 150 microns. In Fig. 4.14, the distribution of isotherms as a function of average convective heat transfer coefficient is shown. Note that the closer the isotherm spacing, the more heat transfer that takes place. Also note that at higher values of the average convective heat transfer coefficient, the cooling effect takes place earlier, closer to the water entrance to the beam. Fig. 4.15 illustrates the effect of increasing the ambient air temperature and water mass flow rate. Again, as one would expect, smaller thermal deflections are realized since the potential for heat transfer between the hot-side surface of the beam and the ambient air is effectly reduced. At 40 g/s, the smallest end thermal deflection occurs, estimated to be about 32 microns, and, as noted before, increasing the water mass flow rate reduces the temperature gradient through the beam and minimizes thermal deflection. In Fig. 4.16, the hot-side surface temperature is reduced to 25 °C and the effects of varying the water mass flow rate is illustrated. In this case, the smallest end thermal deflection, which occurs at 40 g/s, is approximately 25 microns. A comparison of the effect of ambient air temperature is shown in Fig. 4.17. The smallest end deflection, estimated to be about 102 microns,

occurs for an ambient air temperature of 25 °C, compared to an end deflection of about 150 microns for an ambient air temperature of 15 °C.

4.3.5 Maximum Thermal Deflection

The maximum cooling effect occurs at zero water mass flow rate, which results in maximum thermal deflection. Fig. 4.18 is plot of the maximum thermal deflection of the Hydroguide™ bearing as a function of relative humidity. As expected, bone dry air, corresponding to a relative humidity of $\phi = 0$, results in a maximum possible thermal deflection of approximately 395 microns. It should be pointed out that maximum thermal deflection also occurs when the difference between the hot-side surface temperature and ambient air temperature is also a maximum.
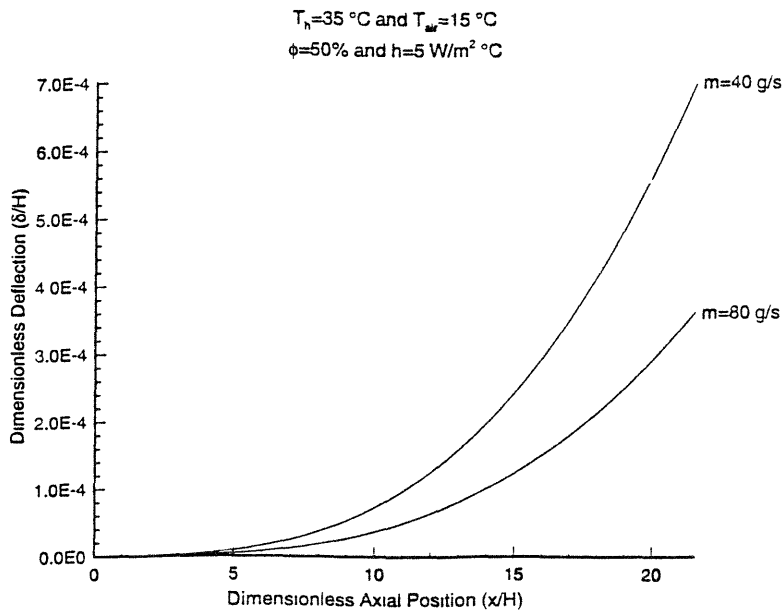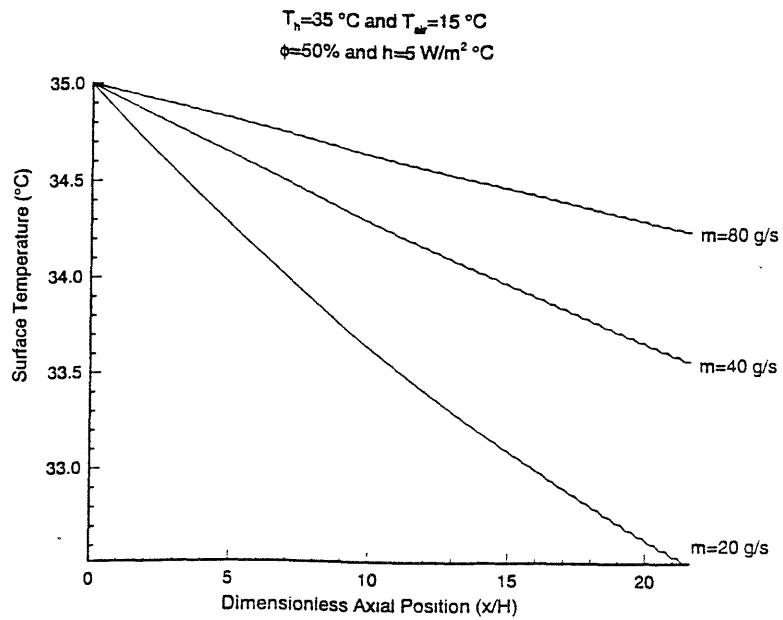
Fig. 4.11 Distribution of cool-side surface temperature and beam thermal deflection as a function of water mass flow rate (2-D).

54

T_h=35 °C and T_{air}=15 °C

h=5 W/m^2 °C, ϕ=50%, m=0.0 (static case)

T_h=35 °C and T_{air}=15 °C

m=10 g/s, ϕ=50%, h=5 W/m^2 °C

T_h=35 °C and T_{air}=15 °C

m=20 g/s, ϕ=50%, h=5 W/m^2 °C

T_h=35 °C and T_{air}=15 °C

m=40 g/s, ϕ=50%, h=5 W/m^2 °C
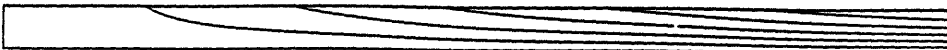
T_h=35 °C and T_{air}=15 °C

m=80 g/s, ϕ=50%, h=5 W/m^2 °C
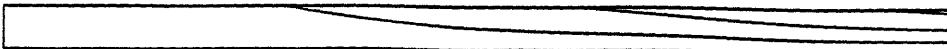
Fig. 4.12 Distribution of isotherms as a function of water mass flow rate (2-D).
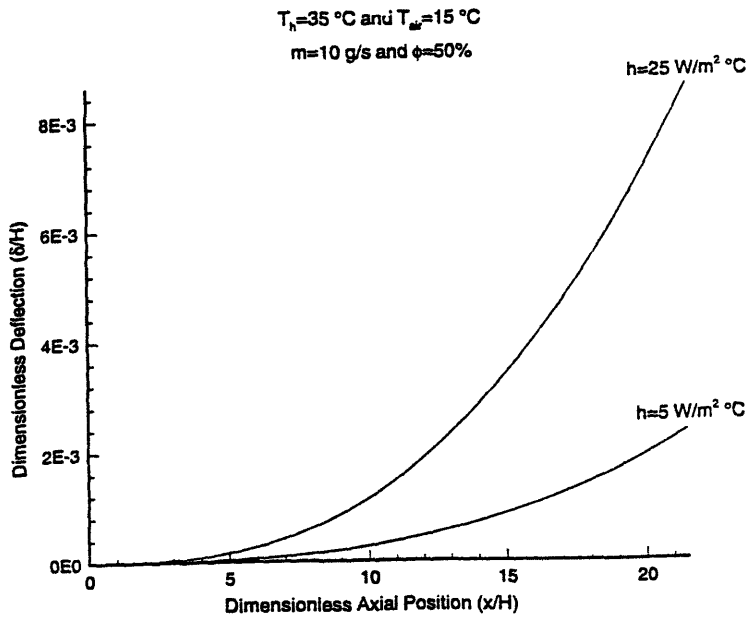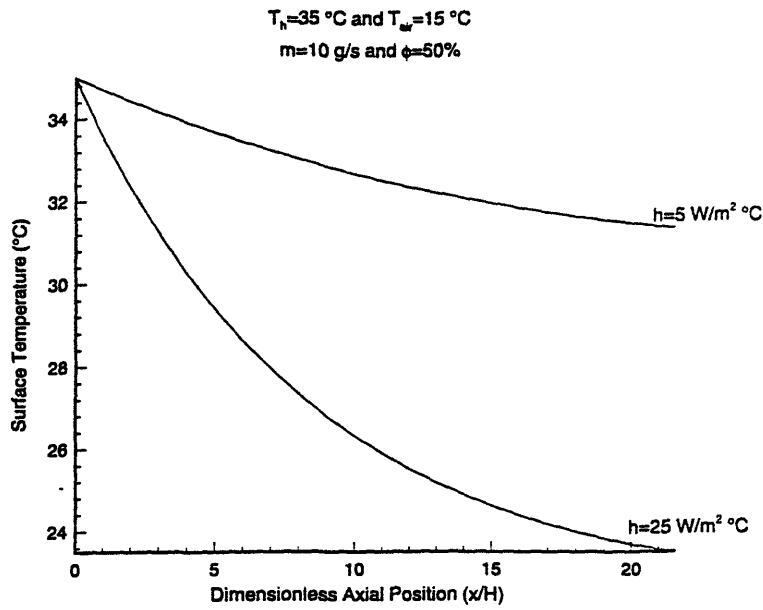
Fig. 4.13 Distribution of cool-side surface temperature and beam thermal deflection as a function of average convective heat transfer coefficient (2-D).

T_h=35 °C and T_{air}=15 °C

m=10 g/s, ϕ=50%, h=5 W/m^2 °C

T_h=35 °C and T_{air}=15 °C

m=10 g/s, ϕ=50%, h=25 W/m^2 °C

Fig. 4.14 Distribution of isotherms as a function of average convective heat transfer coefficient (2-D).
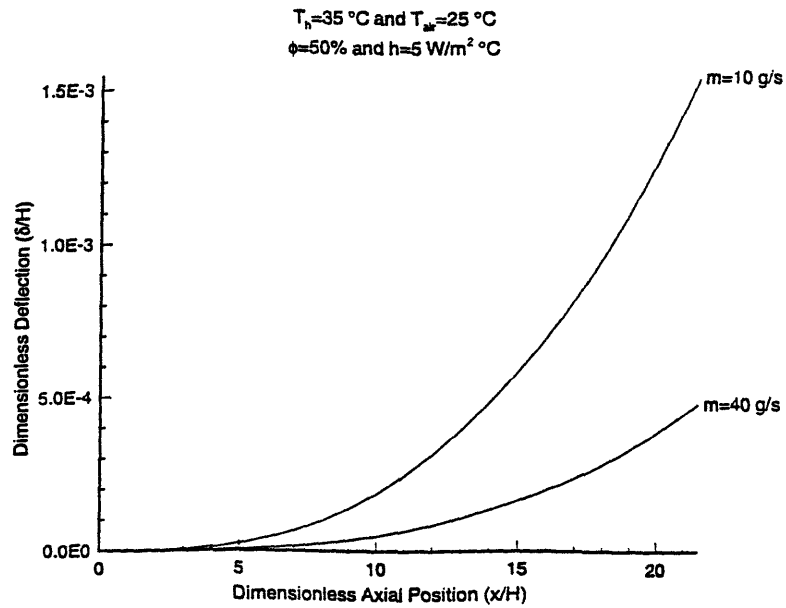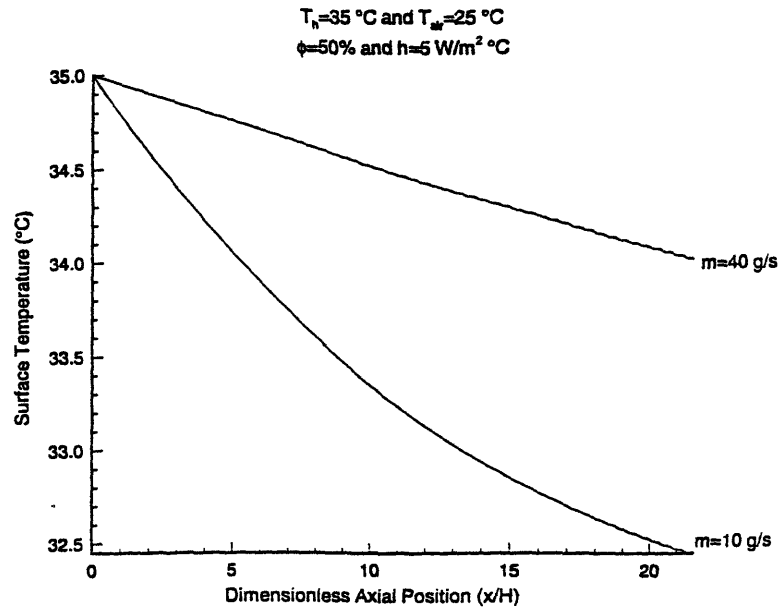
Fig. 4.15 Distribution of cool-side surface temperature and beam thermal deflection as a function of water mass flow rate resulting from higher ambient air temperature (2-D).
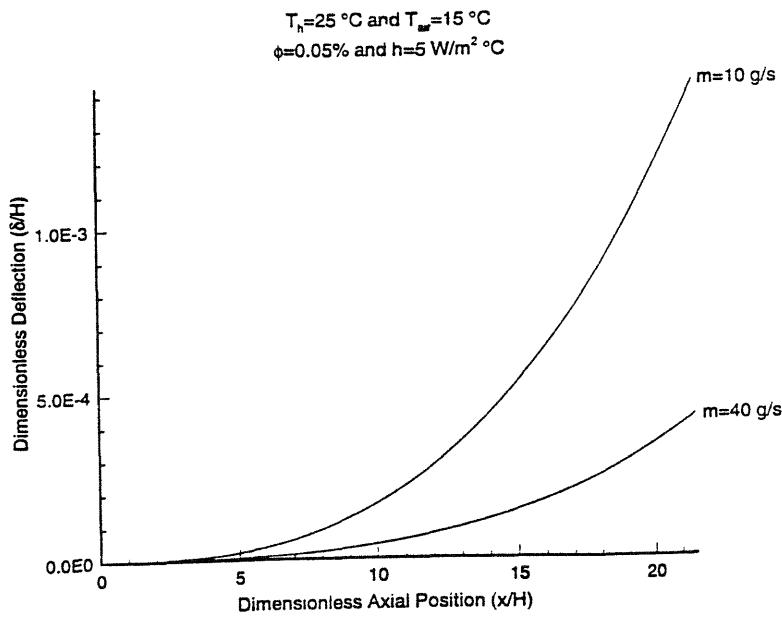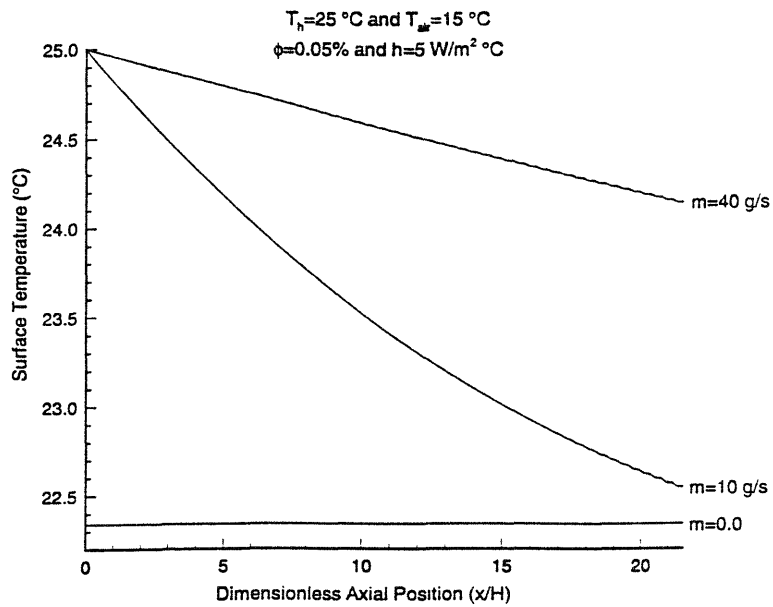
Fig. 4.16 Distribution of cool-side surface temperature and beam thermal deflection as a
function of water mass flow rate resulting from lower hot-side surface temperature (2-D).

59

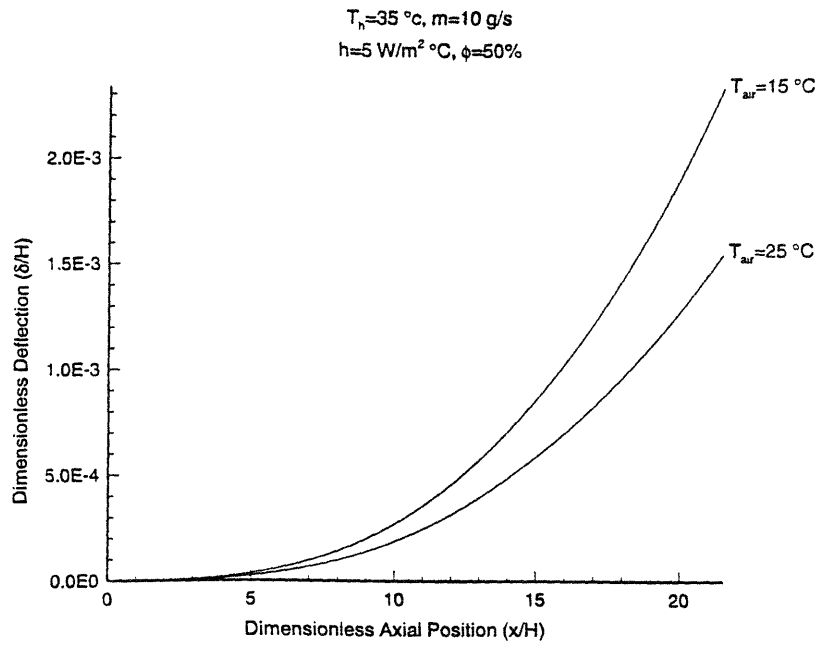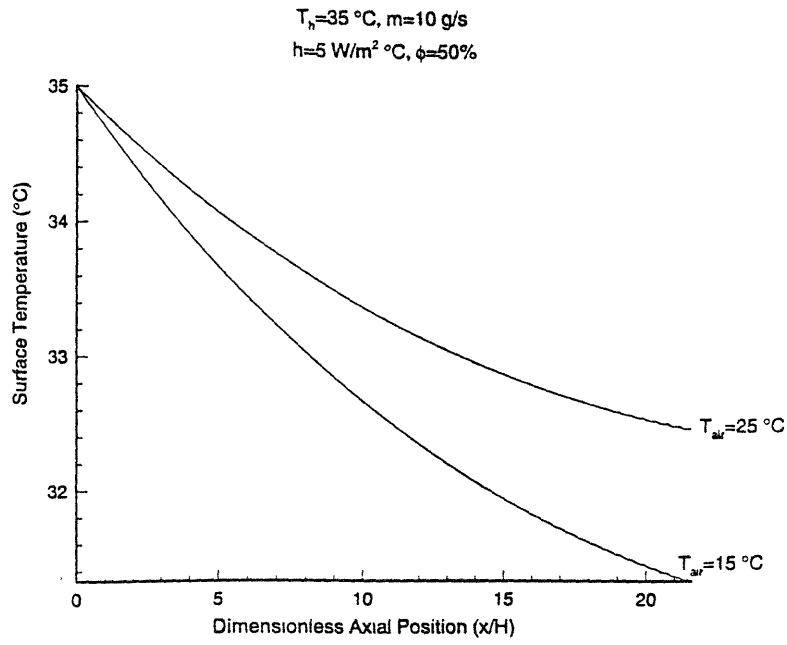Fig. 4.17 Distribution of cool-side surface temperature and beam thermal deflection as a function of ambient air temperature (2-D).
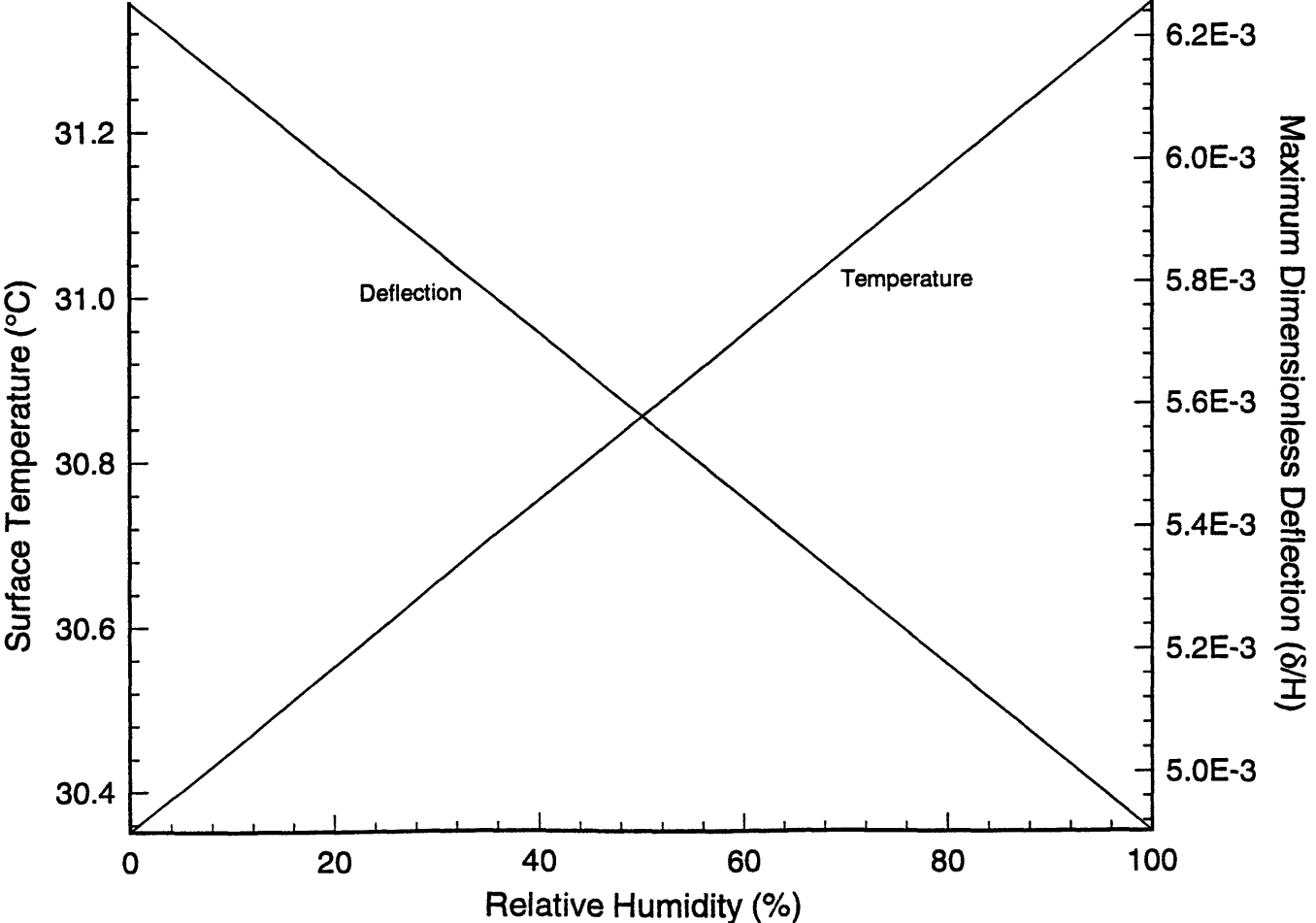
60

Fig. 4.18 Uniform cool-side surface temperature and maximum beam thermal deflection as a function of relative humidity.

Chapter 5

5.1 Conclusions and Design Implications

Analytic and numerical solutions have been presented for the thermal bending errors of precision machine tool members subject to evaporative cooling. Three models have been presented: 1) a hydrostatic model, 2) a 1-D hydrodynamic model, and 3) a 2-D hydrodynamic model. The Hydroguide™ self-compensating, hydrostatic water bearing dimensions and thermophysical properties were used in the results presented for the two hydrodynamic models. The relative effects of the average convective heat transfer coefficient of air across the water layer (5 and 25 W/m² °C), water mass flow rate (in the range: 0 to 80 g/s), ambient air temperature (15, 25, and 35 °C), relative humidity (in the range: 0 to 100 %), and hot-side surface temperature (25 and 35 °C) were studied. The following concluding remarks can made regarding the results contained herein:

1. Maximum thermal deflections occur in the no flow (static) case.

2. Maximum thermal deflections also occur when the ambient air surrounding the machine tool is bone dry (i.e. zero percent relative humidity).

3. Minimum thermal deflections occur when the water mass flow rate is sufficiently high and the machine tool is driven to an isothermal state.

4. High values of the average convective heat transfer coefficient of air results in increased thermal deflection; therefore, free convection effects in the room housing the machine tool should be suppressed.

5. Minimum thermal deflections occur when the difference between the hot-side surface temperature and ambient air temperature is a minimum.

The precision machine tool designer has a monumental task in controlling the environment surrounding the machine tool in order to minimize thermal bending errors. Machine tools should be housed such that wind effects are suppressed and the relative humidity is sufficiently high (greater than about 50%). In addition, the machine tool should be continously flooded at high flow rates in order to drive it to an isothermal state. However, care should be taken not to allow flow leakage along the adiabatic ends since evaporation would tend to cool these surfaces as well. Linear carriages, for example, employing hydrostatic water bearings should be designed such that there is no heat loss from the ends.

5.2 Recommendations for Future Work

The following is a list of recommendations that should be implemented in order to increase the understanding of thermal bending errors in precision machine tools:

1. Extend the models contained herein to three dimensions, including the effects of beam length to height aspect ratio (L/H) and width to height aspect ratio (W/H).

2. Perform analyses with an assortment of boundary conditions, including various inlet water temperatures.

3. Perform analyses for a range of beam materials and clamping conditions.

4. Quantify the relative importance of evaporative cooling at high flow rates as a function of relative humidity.

5. Perform experiments so that analytic and numerical results can be varified.

Bibliography

Cook, R.D. and Young, W.C., *Advanced Mechanics of Materials*, Macmillan, New York, 1985.

Fogiel, M., ed., *The Differential Equations Problem Solver*, Research Education Association, Piscataway, New Jersey, 1991.

Incropera, F.P. and DeWitt, D.P., *Fundamentals of Heat Transfer*, Wiley, New York, 1981.

Jaluria, Y. and Torrance, K.E., *Computational Heat Transfer*, Hemisphere, Washington, D.C., 1986.

Johns, D.J., *Thermal Stress Analysis*, Pergamon Press, New York, 1965.

Lienhard, J.H., *A Heat Transfer Textbook*, Prentice-Hall, Englewood Cliffs, New Jersey, 1987.

Maron, M.J., *Numerical Analysis*, Macmillan, New York, 1987.

Patankar, S.V., *Numerical Heat Transfer and Fluid Flow*, Hemisphere, Washington, D.C., 1980.

Slocum, A.H., *Precision Machine Design*, Prentice-Hall, Englewood Cliffs, New Jersey, 1992.